

# Determining the three-dimensional atomic structure of an amorphous solid

<https://doi.org/10.1038/s41586-021-03354-0>

Received: 10 March 2020

Accepted: 12 February 2021

Published online: 31 March 2021

 Check for updates

Yao Yang<sup>1,6</sup>, Jihan Zhou<sup>1,5,6</sup>, Fan Zhu<sup>1,6</sup>, Yakun Yuan<sup>1,6</sup>, Dillan J. Chang<sup>1</sup>, Dennis S. Kim<sup>1</sup>, Minh Pham<sup>2</sup>, Arjun Rana<sup>1</sup>, Xuezheng Tian<sup>1</sup>, Yonggang Yao<sup>3</sup>, Stanley J. Osher<sup>2</sup>, Andreas K. Schmid<sup>4</sup>, Liangbing Hu<sup>3</sup>, Peter Ercius<sup>4</sup> & Jianwei Miao<sup>1</sup>✉

Amorphous solids such as glass, plastics and amorphous thin films are ubiquitous in our daily life and have broad applications ranging from telecommunications to electronics and solar cells<sup>1–4</sup>. However, owing to the lack of long-range order, the three-dimensional (3D) atomic structure of amorphous solids has so far eluded direct experimental determination<sup>5–15</sup>. Here we develop an atomic electron tomography reconstruction method to experimentally determine the 3D atomic positions of an amorphous solid. Using a multi-component glass-forming alloy as proof of principle, we quantitatively characterize the short- and medium-range order of the 3D atomic arrangement. We observe that, although the 3D atomic packing of the short-range order is geometrically disordered, some short-range-order structures connect with each other to form crystal-like superclusters and give rise to medium-range order. We identify four types of crystal-like medium-range order—face-centred cubic, hexagonal close-packed, body-centred cubic and simple cubic—coexisting in the amorphous sample, showing translational but not orientational order. These observations provide direct experimental evidence to support the general framework of the efficient cluster packing model for metallic glasses<sup>10,12–14,16</sup>. We expect that this work will pave the way for the determination of the 3D structure of a wide range of amorphous solids, which could transform our fundamental understanding of non-crystalline materials and related phenomena.

Since their discovery in 1960<sup>17</sup>, metallic glasses have been actively studied for fundamental interest and practical applications<sup>9–16,18–21</sup>. However, owing to their disordered structure, the 3D atomic arrangement of metallic glasses cannot be determined by crystallography<sup>22</sup>. Over the years, a number of experimental and computational methods have been used to study the metallic-glass structure, such as X-ray and neutron diffraction<sup>23,24</sup>, X-ray absorption fine structure<sup>11</sup>, high-resolution transmission electron microscopy<sup>25</sup>, fluctuation electron microscopy<sup>26</sup>, ångström- and nano-beam electron diffraction<sup>15,27,28</sup>, nuclear magnetic resonance<sup>29</sup>, density functional theory<sup>30</sup>, molecular dynamics simulations<sup>31–34</sup> and reverse Monte Carlo modelling<sup>11,26</sup>. Despite all these developments, however, no experimental method has been able to directly determine all the 3D atomic positions in metallic-glass samples. One experimental method that can in principle solve this long-standing problem is atomic electron tomography (AET)<sup>35,36</sup>. AET combines high-resolution tomographic tilt series with advanced iterative algorithms to resolve the 3D atomic structure of materials without assuming crystallinity, which has been applied to image grain boundaries, anti-phase boundaries, stacking faults, dislocations, point defects, chemical order/disorder, atomic-scale ripples, bond distortion and strain tensors with unprecedented 3D detail<sup>37–42</sup>. More recently, four-dimensional (three

dimensions and time) AET has been developed to observe crystal nucleation at atomic resolution, showing that early-stage nucleation results are inconsistent with classical nucleation theory<sup>43</sup>. Here, we use an amorphous sample of a glass-forming alloy as a model and improve AET to determine the alloy's 3D atomic positions with a precision of 21 pm.

## 3D atomic positions in a glass-forming alloy

The samples were synthesized by a carbothermal shock technique with a high cooling rate (Extended Data Fig. 1a, Supplementary Video 1, Methods), which was used to create high-entropy-alloy nanoparticles with multi-metal components<sup>44</sup>. Energy-dispersive X-ray (EDX) spectroscopy data show that the nanoparticles are composed of eight elements: Co, Ni, Ru, Rh, Pd, Ag, Ir and Pt (Extended Data Fig. 1b–k). Tomographic tilt series were acquired from seven nanoparticles using an annular dark-field scanning transmission electron microscope (Extended Data Table 1). Although most of the nanoparticles are crystalline or polycrystalline, particles 1 and 2 have disordered structure (Extended Data Fig. 2). In this study, we focus on the most disordered nanoparticle (particle 1), from which a tilt series of 55 images was acquired (Fig. 1a, Extended Data Fig. 3). Although some crystalline features are present

<sup>1</sup>Department of Physics & Astronomy, STROBE NSF Science & Technology Center and California NanoSystems Institute, University of California, Los Angeles, CA, USA. <sup>2</sup>Department of Mathematics, University of California, Los Angeles, CA, USA. <sup>3</sup>Department of Materials Science and Engineering, University of Maryland, College Park, MD, USA. <sup>4</sup>National Center for Electron Microscopy, Molecular Foundry, Lawrence Berkeley National Laboratory, Berkeley, CA, USA. <sup>5</sup>Present address: Beijing National Laboratory for Molecular Sciences, College of Chemistry and Molecular Engineering, Peking University, Beijing, P. R. China. <sup>6</sup>These authors contributed equally: Yao Yang, Jihan Zhou, Fan Zhu, Yakun Yuan. ✉e-mail: miao@physics.ucla.edu

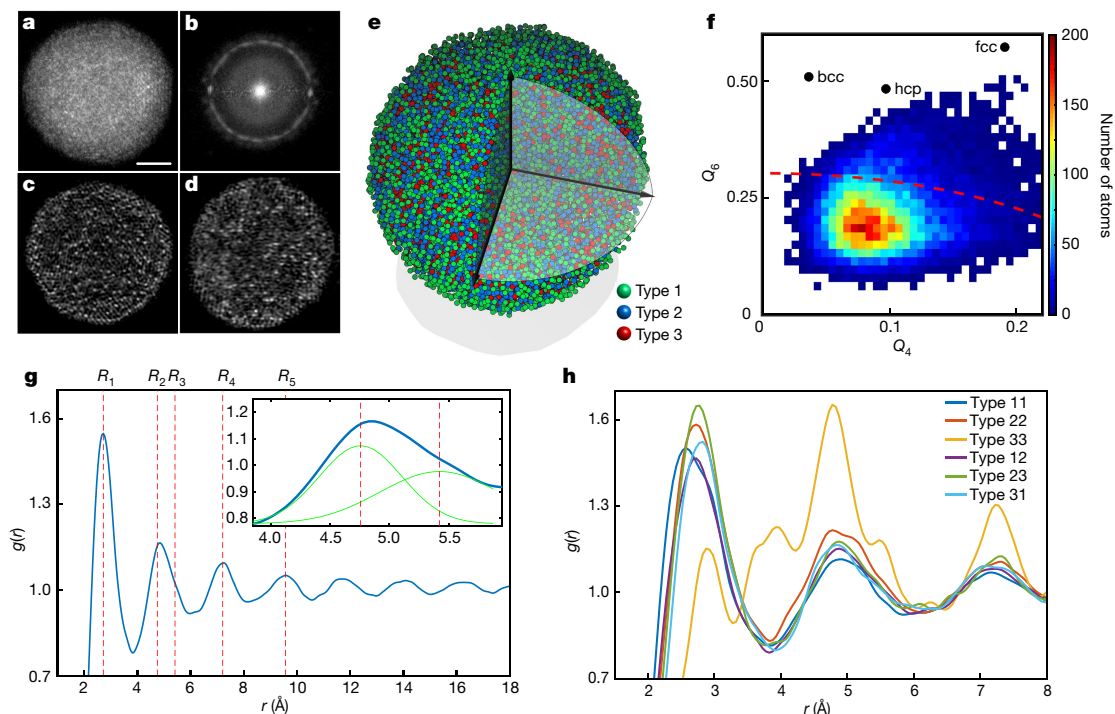


**Fig. 1 | Determining the 3D atomic structure of a multi-component glass-forming nanoparticle with AET.** **a**, Representative experimental image, where some crystalline features are visible. Scale bar, 2 nm. **b**, Average 2D power spectrum of 55 experimental images (Extended Data Fig. 3), showing the amorphous halo. **c, d**, Two 2.4-Å-thick slices of the 3D reconstruction in the  $x$ - $y$  (**c**) and  $y$ - $z$  (**d**) plane, where the majority of type-3 atoms (bright dots) are distributed in the second coordination shell. **e**, Experimental 3D atomic model of the glass-forming nanoparticle. **f**, Local BOO parameters of all the atoms in the

nanoparticle. According to the criterion of the normalized BOO parameter being  $<0.5$  (dashed red curve), 84.54% of the total atoms are disordered. **g**, PDF of the disordered atoms, with the first, second, third, fourth and fifth peak positions at  $R_1 = 2.73 \text{ \AA}$ ,  $R_2 = 4.76 \text{ \AA}$ ,  $R_3 = 5.42 \text{ \AA}$ ,  $R_4 = 7.22 \text{ \AA}$  and  $R_5 = 9.57 \text{ \AA}$ , respectively. The inset shows the second-peak splitting with a double Gaussian fit.  $r$ , radial distance. **h**, Partial PDFs between type-1, -2 and -3 atoms consisting of six pairs—types 11, 12, 13, 22, 23 and 33. The partial PDF for the type-33 pairs (yellow curve) shows a unique feature, with a second peak higher than the first peak.

in several images, the two-dimensional (2D) power spectra calculated from the images show the amorphous halo (Fig. 1b).

After pre-processing and image denoising, the tilt series was reconstructed and the 3D atomic positions were traced and classified (Fig. 1c, d, Supplementary Video 2, Methods). Because the image contrast in the 3D reconstruction depends on the atomic number<sup>41–43</sup>, at present AET is only sensitive enough to classify the eight elements into three different types: Co and Ni as type 1; Ru, Rh, Pd and Ag as type 2; and Ir and Pt as type 3. After atom classification, we obtained the 3D atomic model of the nanoparticle, consisting of 8,322, 6,896 and 3,138 atoms of type 1, 2 and 3, respectively. To verify the reconstruction, atom tracing and classification procedure, we generated 55 images from the experimental atomic model using multi-slice simulations (Methods). Extended Data Fig. 4c, d shows the consistency between the experimental and generated images. We then applied the reconstruction, atom tracing and classification procedure to obtain a new 3D atomic model from the 55 multi-slice images. By comparing the two models, we estimated that 97.37% of atoms were correctly identified with a 3D precision of 21 pm (Methods, Extended Data Fig. 4e).

Figure 1e and Supplementary Video 3 show the experimental 3D atomic model of the nanoparticle, with type-1, -2 and -3 atoms in green, blue and red, respectively. To quantitatively characterize the atomic structure, we employed the local bond orientational order (BOO) parameters to distinguish between the disordered, face-centred cubic (fcc), hexagonal close-packed (hcp) and body-centred cubic (bcc) structures (Methods). Figure 1f shows the local BOO parameters of all the atoms in the nanoparticle, indicating that the majority of atoms deviate markedly from the fcc, hcp and bcc crystal structures. For comparison, the local BOO parameters of all seven nanoparticles are shown in Extended Data Fig. 2h–n. To separate crystal nuclei from

the amorphous structure, we used the normalized BOO parameter to identify the crystal nuclei (Methods). Using the criterion that the normalized BOO parameter is  $\geq 0.5$  (Extended Data Fig. 2o), we identified 15.46% of the total atoms forming crystal nuclei in the nanoparticle (Extended Data Fig. 5a), which contribute to the crystalline features observed in several images (Extended Data Fig. 3). The characteristic width of the crystalline–amorphous interface in the nanoparticle was determined to be 3.69 Å (Methods), indicating that the crystal nuclei have a minimal effect on the structural disorder beyond a few ångströms. In the following sections, we focus on the analysis of disordered atoms with normalized BOO parameter  $<0.5$ .

Figure 1g shows the pair distribution function (PDF) of the amorphous structure of the 3D atomic model (Methods), where the weak second-peak splitting is consistent with previous observations in high-entropy bulk metallic glasses<sup>45</sup>. The ratios of the second, third, fourth and fifth peak positions to that of the first peak are 1.74, 1.99, 2.64 and 3.51, respectively, which are in good agreement with those of metallic glasses<sup>46,47</sup>. The partial PDFs between type-1, -2 and -3 atoms are shown in Fig. 1h. By fitting a Gaussian to the first peaks in the partial PDFs, we determined the type-11, -12, -13, -22, -23 and -33 bond lengths to be 2.59, 2.71, 2.78, 2.72, 2.75 and 2.9 Å, respectively. In particular, the partial PDF for the type-33 pairs (the yellow curve) exhibits a unique feature, with the second peak being higher than the first one, indicating that the majority of type-3 atoms are distributed beyond the short-range order (SRO).

### The short-range order

To determine the SRO in the glass-forming nanoparticle, we used the Voronoi tessellation to characterize the local atomic arrangement<sup>8</sup>.

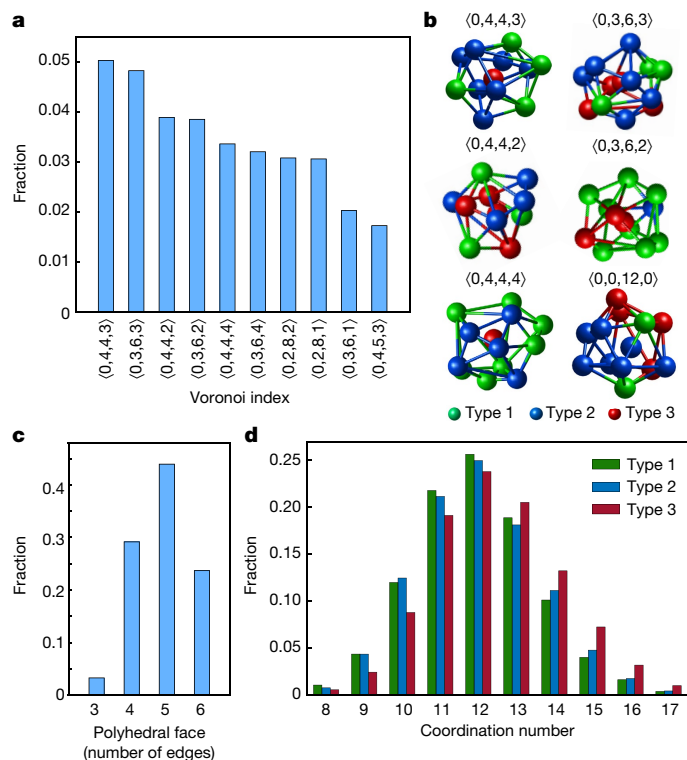


**Fig. 2 | SRO of the glass-forming nanoparticle.** **a**, Ten most abundant Voronoi polyhedra in the nanoparticle. **b**, Six representative Voronoi polyhedra, where  $\langle 0, 4, 4, 3 \rangle$ ,  $\langle 0, 3, 6, 3 \rangle$ ,  $\langle 0, 4, 4, 2 \rangle$  and  $\langle 0, 3, 6, 2 \rangle$  are the four highest-fraction Voronoi indices,  $\langle 0, 4, 4, 4 \rangle$  indicates a severely distorted polyhedron, and  $\langle 0, 0, 12, 0 \rangle$  represents an icosahedron. **c**, The 3-, 4-, 5- and 6-edged face distribution of all the Voronoi polyhedra, where the 5-edged faces are the most abundant (43.91%). **d**, Coordination number distributions for type-1, -2 and -3 atoms.

This method identifies the nearest-neighbour atoms around each central atom to form a Voronoi polyhedron, which is designated by a Voronoi index  $\langle n_3, n_4, n_5, n_6 \rangle$ , with  $n_i$  denoting the number of  $i$ -edged faces. Figure 2a shows the ten most abundant Voronoi polyhedra in the nanoparticle with a fraction ranging from 5.02% to 1.72%, most of which are geometrically disordered and typically observed in model metallic glasses<sup>13</sup> such as  $\langle 0, 4, 4, 3 \rangle$ ,  $\langle 0, 3, 6, 3 \rangle$ ,  $\langle 0, 4, 4, 2 \rangle$  and  $\langle 0, 3, 6, 2 \rangle$  (Fig. 2b). To examine the effect of the precision of AET on the Voronoi analysis, we added the experimental error (Extended Data Fig. 4e) to a  $\text{Cu}_{65}\text{Zr}_{35}$  metallic-glass model obtained from molecular dynamics simulations. By comparing the Voronoi polyhedra with and without the error, we found that the precision of AET has only a small effect on the Voronoi tessellation (Methods). This result suggests that the small fractions of the Voronoi polyhedra in the glass-forming nanoparticle are mainly due to its poor glass-forming ability<sup>13,20</sup>.

Figure 2c shows the local symmetry distribution of all the faces of the Voronoi polyhedra. The 3-, 4-, 5- and 6-edged faces account for 3.27%, 29.14%, 43.91% and 23.67%, respectively, revealing that 5-edged faces are most abundant in the SRO. However, only 7.03% of all the Voronoi polyhedra are distorted icosahedra, including Voronoi indices  $\langle 0, 0, 12, 0 \rangle$ ,  $\langle 0, 1, 10, 2 \rangle$ ,  $\langle 0, 2, 8, 2 \rangle$  and  $\langle 0, 2, 8, 1 \rangle$ . This observation indicates that most 5-edged faces do not form distorted icosahedra in this glass-forming nanoparticle. From the Voronoi tessellation, we also calculated the distribution of the coordination number (Fig. 2d and Methods), and the average coordination numbers of type 1, 2 and 3 atoms are 11.97, 12.02 and 12.41, respectively. On the basis of the partial coordination numbers (Extended Data Fig. 5b), we quantified the chemical SRO using the Warren–Cowley parameters (Methods), which indicated that type-11 and -23 bonds are favoured but type-12 and -33 bonds are disfavoured. These results are consistent with the observations of the shortening of type-11 and -23 bonds and the lengthening of type-12 and -33 bonds (Methods).

### The medium-range order

Although medium-range order (MRO) in metallic glasses is broadly defined as the nanometre-scale structural organization beyond the

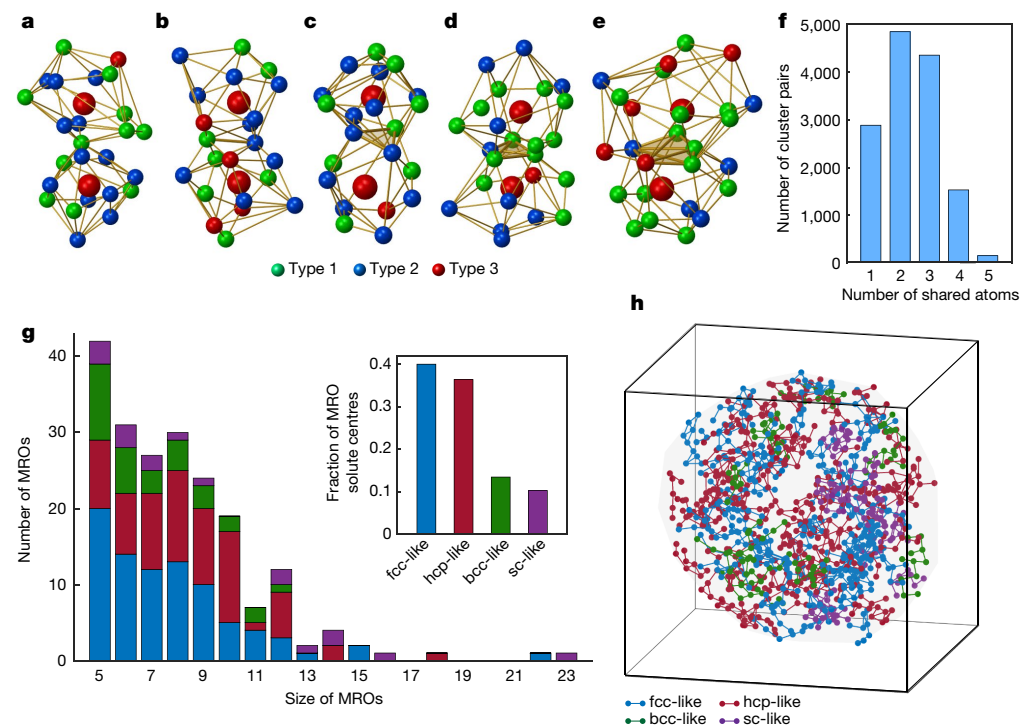


**Fig. 3 | Connectivity and distribution of MROs in the glass-forming nanoparticle.** **a–e**, Representative pairs of solute-centre clusters connected with each other by sharing one (**a**), two (**b**), three (**c**), four (**d**) and five (**e**) atoms, where the central atom of each cluster is shown as a large red sphere. **f**, Statistical distribution of the number of solute-centre cluster pairs that share 1–5 atoms. **g**, Histogram of the four types of MRO—fcc- (blue), hcp- (red), bcc- (green) and sc-like (purple)—as a function of size (that is, the number of solute centres). The total number of fcc-, hcp-, bcc- and sc-like MROs is 85, 71, 31 and 17, respectively. The inset shows the fraction of solute-centre atoms in the four types of MRO. **h**, Distribution of the four types of MRO with eight solute-centre atoms or more, where the central region lacks large MROs.

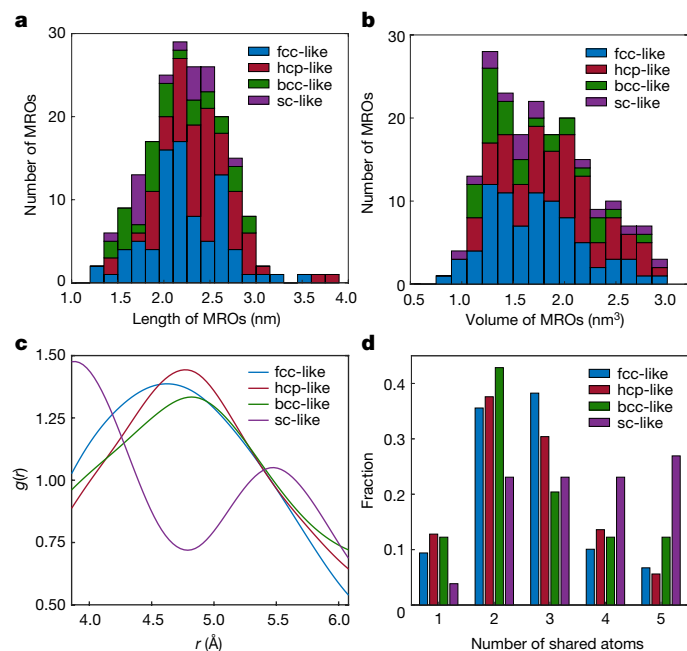


**Fig. 4 | Quantitative characterization of MROs.** **a, b**, Length (**a**) and volume (**b**) distribution of the four types of MRO in the glass-forming nanoparticle, where the length was measured along the longest direction of each MRO. **c**, Partial PDFs of the fcc-, hcp-, bcc- and sc-like solute centres in the glass-forming nanoparticle, where the maximum peak positions are located at 4.62, 4.77, 4.82 and 3.88 Å, respectively. Compared with the other three partial PDFs, the partial PDF of the sc-like solute centres (purple curve) shows two peaks with a ratio of the second to the first peak position of about  $\sqrt{2}$ . **d**, Histogram of neighbouring solute-centre clusters sharing one, two, three, four and five atoms for the four types of MRO.

SRO<sup>10–16,26,27,32</sup>, in this work we focused on the investigation of the MRO in the framework of the efficient cluster packing model<sup>10,14</sup>. This model hypothesizes that solute atoms are surrounded by randomly positioned solvent atoms to form solute-centre clusters that are densely packed to constitute crystal-like MROs in metallic glasses. To quantitatively test this model with experimental data, we analysed the partial PDF of type-33 atom pairs (Fig. 1h, yellow curve) and observed that the highest peak is at 4.77 Å and 1.49 times higher than the nearest-neighbour peak. We found that 85.47% of type-3 atoms are distributed in the second coordination shell (Extended Data Fig. 5c, Methods), which is between the first (3.86 Å) and the second (6.08 Å) minimum of the PDF curve (Fig. 1g). These type-3 atoms act as solute atoms and are surrounded mainly by type-1 and -2 solvent atoms to form solute-centre clusters. Extended Data Fig. 5d shows the ten most abundant Voronoi polyhedra of these clusters. The solute-centre clusters connect with each other by sharing one (a vertex), two (an edge), three (a face), four and five atoms (Fig. 3a–e). Figure 3f shows the statistical distribution of the number of solute-centre cluster pairs sharing from one to five atoms.

To locate the MRO in the glass-forming nanoparticle, we implemented a breadth-first search algorithm to look for the fcc-, hcp-, bcc-, simple cubic (sc-) and icosahedral-like structures of the solute centres (Methods). This algorithm searches globally for MRO with the maximum number of solute centres. Each MRO is defined to have five or more solute centres, with each solute centre falling within a 0.75-Å radius of the fcc, hcp, bcc, sc lattice or icosahedral vertices. We found that four types of MRO (fcc-, hcp-, bcc- and sc-like) coexist in the sample (Methods). Although we did not observe icosahedral-like MROs in this sample, our work does not rule out its existence in other metallic glasses<sup>11</sup>. Figure 3g shows a histogram of the four types of MRO as a function of size, and the inset illustrates the fraction of the solute-centre atoms in the four types of MRO. Figure 3h and Supplementary Video 4

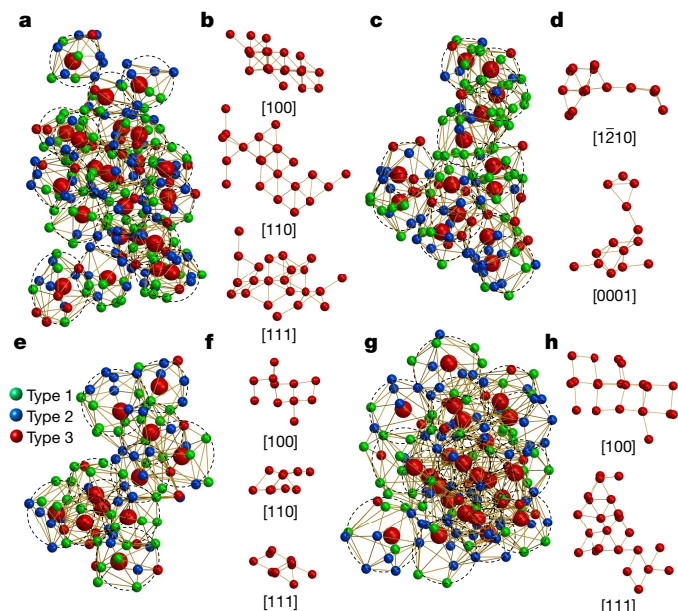


**Fig. 5 | 3D atomic packing of four representative MROs.** **a–h**, Representative fcc- (**a**), hcp- (**c**), bcc- (**e**) and sc-like (**g**) MROs, consisting of 22, 14, 11 and 23 solute centres (large red spheres), respectively, where the individual solute-centre clusters (dashed circles) are randomly oriented. To better visualize the crystal-like MROs, the solvent atoms have been removed and the solute centres are orientated along the fcc (**b**), hcp (**d**), bcc (**f**) and sc (**h**) zone axes, showing that the MROs have anisotropic 3D shapes and strongly deviate from the crystal lattices.

show the 3D distribution of MROs having eight solute centres or more. To verify our analysis, we also searched for MROs with a 1-Å and 0.5-Å radius cut-off, and observed coexistence of the four types of MRO with different cut-off radii (Extended Data Figs. 6, 7).

Next, we quantitatively characterized MROs with a 0.75-Å radius cut-off. Figure 4a, b shows the length and volume distribution of the MROs in the glass-forming nanoparticle. The average length of the fcc-, hcp-, bcc- and sc-like MROs was measured to be  $2.27 \pm 0.50$ ,  $2.40 \pm 0.42$ ,  $2.07 \pm 0.38$ ,  $2.11 \pm 0.48$  nm, respectively, with corresponding average volume of  $1.80 \pm 0.64$ ,  $1.96 \pm 0.53$ ,  $1.63 \pm 0.46$  and  $1.96 \pm 0.74$  nm<sup>3</sup>. Figure 5a, c, e, g shows four representative fcc-, hcp-, bcc- and sc-like MROs, in which the solute-centre clusters exhibit only translational but not orientational order. To better visualize these MROs, the solute centres are orientated along the fcc, hcp, bcc and sc zone axes (Fig. 5b, d, f, h), showing that the 3D shapes of the MROs are anisotropic. We calculated the partial PDFs of all the fcc-, hcp-, bcc- and sc-like solute centres in the glass-forming nanoparticle, and their corresponding maximum peak positions are at 4.62, 4.77, 4.82 and 3.88 Å, respectively (Fig. 4c). These peak positions represent the average nearest-neighbour distances of the solute centres in the four crystal-like MROs, and the broadened peaks signify the severe deviation from the crystal lattices. Compared with the other three partial PDFs, the partial PDF of the sc-like MROs has two peaks, and the ratio of the second to the first peak position is about  $\sqrt{2}$  (Fig. 4c, purple curve), which corresponds to the ratio of the diagonal to the side length of a square. The shorter nearest-neighbour distance of the sc-like MROs compared to the other three crystal-like MROs indicates that the sc-like solute-centre clusters are more closely connected with their neighbours. Figure 4d shows the histogram of sharing one, two, three, four and five atoms between neighbouring solute-centre clusters for the four types of MRO, confirming that the solute-centre clusters in the sc-like MROs tend to share more atoms with their neighbours than those in other types of MRO.

Our quantitative analysis of the SRO and MRO in a multi-component glass-forming nanoparticle provides direct experimental evidence to support the general framework of the efficient cluster-packing model<sup>10,12–14,16</sup>; that is, solute-centre clusters are densely packed in some parts of the sample to form crystal-like MROs. We observed chemical SRO, bond shortening and lengthening, and coexistence of fcc-, hcp-, bcc- and sc-like MROs in the glass-forming nanoparticle. By quantifying their length, volume and 3D structure, we found that the MRO not only has a large variation in length and volume, but also severely deviates from the crystal lattices (Fig. 4c). As the size of the MRO is comparable to that of shear transformation zones in metallic glasses<sup>13,16,48,49</sup>, we expect that AET could also be applied to determine the 3D atomic structures that are related to shear transformation zones and link the structure and properties of metallic glasses<sup>13</sup>.

## Outlook

Over the last century, crystallography has been broadly applied to determine the 3D atomic structure of crystalline samples<sup>22</sup>. The quantitative 3D structural information has been fundamental to the development of many scientific fields. However, for amorphous solids, their 3D structure has been primarily inferred from experimental data, where either the average statistical structural information can be obtained or model fitting is required to analyse the local atomic order<sup>10–15</sup>. These qualitative approaches have hindered our fundamental understanding of the 3D structure of amorphous solids and related phenomena, such as the crystal–amorphous phase transition and the glass transition<sup>13,50,51</sup>. Here, we demonstrate the ability to directly determine the 3D atomic structure of an amorphous solid using AET, which enables us to quantitatively analyse the SRO and MRO at the single-atom level. Although we focus on a multi-component glass-forming nanoparticle, this method is generally applicable to different sample geometries, such as thin films and extended objects (Extended Data Figs. 8, 9, Methods). Therefore, we expect that this work could open a new era in determining the 3D structure of a wide range of amorphous solids.

## Online content

Any methods, additional references, Nature Research reporting summaries, source data, extended data, supplementary information, acknowledgements, peer review information; details of author contributions and competing interests; and statements of data and code availability are available at <https://doi.org/10.1038/s41586-021-03354-0>.

- Zallen, R. *The Physics of Amorphous Solids* (Wiley, 1998).
- Elliott, S. R. *Physics of Amorphous Materials* (Longman Scientific & Technical, 1990).
- Andrady, A. L. & Neal, M. A. Applications and societal benefits of plastics. *Phil. Trans. R. Soc. B* **364**, 1977–1984 (2009).
- Carlson, D. E. & Wronski, C. R. Amorphous silicon solar cell. *Appl. Phys. Lett.* **28**, 671–673 (1976).
- Zachariasen, W. H. The atomic arrangement in glass. *J. Am. Chem. Soc.* **54**, 3841–3851 (1932).
- Bernal, J. D. & Mason, J. Packing of spheres: co-ordination of randomly packed spheres. *Nature* **188**, 910–911 (1960).
- Scott, G. D. Packing of equal spheres. *Nature* **188**, 908–909 (1960).
- Finney, J. L. Random packings and structure of simple liquids. I. Geometry of random close packing. *Proc. R. Soc. Lond. A* **319**, 479–493 (1970).
- Nelson, D. R. & Spaepen, F. Polytetrahedral order in condensed matter. *Solid State Phys.* **42**, 1–90 (1989).
- Miracle, D. B. A structural model for metallic glasses. *Nat. Mater.* **3**, 697–702 (2004).
- Sheng, H. W., Luo, W. K., Alamgir, F. M., Bai, J. M. & Ma, E. Atomic packing and short-to-medium-range order in metallic glasses. *Nature* **439**, 419–425 (2006).
- Miracle, D. B., Egami, T., Flores, K. M. & Kelton, K. F. Structural aspects of metallic glasses. *MRS Bull.* **32**, 629–634 (2007).

- Cheng, Y. Q. & Ma, E. Atomic-level structure and structure-property relationship in metallic glasses. *Prog. Mater. Sci.* **56**, 379–473 (2011).
- Miracle, D. B. A physical model for metallic glass structures: an introduction and update. *JOM* **64**, 846–855 (2012).
- Hirata, A. et al. Geometric frustration of icosahedron in metallic glasses. *Science* **341**, 376–379 (2013).
- Chen, M. W. A brief overview of bulk metallic glasses. *NPG Asia Mater.* **3**, 82–90 (2011).
- Klement Jun, W., Willens, R. H. & Duwez, P. Non-crystalline structure in solidified gold-silicon alloys. *Nature* **187**, 869–870 (1960).
- Greer, A. L. Metallic glasses. *Science* **267**, 1947–1953 (1995).
- Peker, A. & Johnson, W. L. A highly processable metallic glass:  $Zr_{41.2}Ti_{13.8}Cu_{12.5}Ni_{10.0}Be_{22.5}$ . *Appl. Phys. Lett.* **63**, 2342–2344 (1993).
- Inoue, A. Stabilization of metallic supercooled liquid and bulk amorphous alloys. *Acta Mater.* **48**, 279–306 (2000).
- Wang, W. H., Dong, C. & Shek C. H. Bulk metallic glasses. *Mater. Sci. Eng. Rep.* **44**, 45–89 (2004).
- Giacovazzo, C. et al. *Fundamentals of Crystallography* 3rd edn (Oxford Univ. Press, 2011).
- Egami, T. & Billinge, S. J. L. *Underneath the Bragg Peaks: Structural Analysis of Complex Materials* (Pergamon, 2003).
- Kelton, K. F. et al. First X-ray scattering studies on electrostatically levitated metallic liquids: demonstrated influence of local icosahedral order on the nucleation barrier. *Phys. Rev. Lett.* **90**, 195504 (2003).
- Zhong, L., Wang, J., Sheng, H., Zhang, Z. & Mao, S. X. Formation of monatomic metallic glasses through ultrafast liquid quenching. *Nature* **512**, 177–180 (2014).
- Hwang, J. et al. Nanoscale structure and structural relaxation in  $Zr_{50}Cu_{48}Ag_2$  bulk metallic glass. *Phys. Rev. Lett.* **108**, 195505 (2012).
- Hirata, A. et al. Direct observation of local atomic order in a metallic glass. *Nat. Mater.* **10**, 28–33 (2011).
- Pekin, T. C. et al. Direct measurement of nanostructural change during in situ deformation of a bulk metallic glass. *Nat. Commun.* **10**, 2445 (2019).
- Tang, X. P., Geyer, U., Busch, R., Johnson, W. L. & Wu, Y. Diffusion mechanisms in metallic supercooled liquids and glasses. *Nature* **402**, 160–162 (1999).
- Sachdev, S. & Nelson, D. R. Order in metallic glasses and icosahedral crystals. *Phys. Rev. B* **32**, 4592–4606 (1985).
- Tang, C. & Harrowell, P. Anomalously slow crystal growth of the glass-forming alloy CuZr. *Nat. Mater.* **12**, 507–511 (2013).
- Cheng, Y. Q., Ma, E. & Sheng, H. W. Atomic level structure in multicomponent bulk metallic glass. *Phys. Rev. Lett.* **102**, 245501 (2009).
- Hu, Y. C., Li, F. X., Li, M. Z., Bai, H. Y. & Wang, W. H. Five-fold symmetry as indicator of dynamic arrest in metallic glass-forming liquids. *Nat. Commun.* **6**, 8310 (2015).
- Ding, J. & Ma, E. Computational modeling sheds light on structural evolution in metallic glasses and supercooled liquids. *npl Comput. Mater.* **3**, 9 (2017).
- Scott, M. C. et al. Electron tomography at 2.4-ångström resolution. *Nature* **483**, 444–447 (2012).
- Miao, J., Ercius, P. & Billinge, S. J. L. Atomic electron tomography: 3D structures without crystals. *Science* **353**, aaf2157 (2016).
- Chen, C.-C. et al. Three-dimensional imaging of dislocations in a nanoparticle at atomic resolution. *Nature* **496**, 74–77 (2013).
- Goris, B. et al. Three-dimensional elemental mapping at the atomic scale in bimetallic nanocrystals. *Nano Lett.* **13**, 4236–4241 (2013).
- Xu, R. et al. Three-dimensional coordinates of individual atoms in materials revealed by electron tomography. *Nat. Mater.* **14**, 1099–1103 (2015).
- Haberfehlner, G. et al. Formation of bimetallic clusters in superfluid helium nanodroplets analysed by atomic resolution electron tomography. *Nat. Commun.* **6**, 8779 (2015).
- Yang, Y. et al. Deciphering chemical order/disorder and material properties at the single-atom level. *Nature* **542**, 75–79 (2017).
- Tian, X. et al. Correlating the three-dimensional atomic defects and electronic properties of two-dimensional transition metal dichalcogenides. *Nat. Mater.* **19**, 867–873 (2020).
- Zhou, J. et al. Observing crystal nucleation in four dimensions using atomic electron tomography. *Nature* **570**, 500–503 (2019).
- Yao, Y. et al. Carbothermal shock synthesis of high-entropy-alloy nanoparticles. *Science* **359**, 1489–1494 (2018).
- Kim, J. Y. et al. Utilization of high entropy alloy characteristics in Er-Gd-Y-Al-Co high entropy bulk metallic glass. *Acta Mater.* **155**, 350–361 (2018).
- Liu, X. J. et al. Metallic liquids and glasses: atomic order and global packing. *Phys. Rev. Lett.* **105**, 155501 (2010).
- Wu, Z. W., Li, M. Z., Wang, W. H. & Liu, K. X. Hidden topological order and its correlation with glass-forming ability in metallic glasses. *Nat. Commun.* **6**, 6035 (2015).
- Spaepen, F. A microscopic mechanism for steady state inhomogeneous flow in metallic glasses. *Acta Metall.* **25**, 407–415 (1977).
- Argon, A. S. Plastic-deformation in metallic glasses. *Acta Metall.* **27**, 47–58 (1979).
- Johnson, W. L. Thermodynamic and kinetic aspects of the crystal to glass transformation in metallic materials. *Prog. Mater. Sci.* **30**, 81–134 (1986).
- Debenedetti, P. G. & Stillinger, F. H. Supercooled liquids and the glass transition. *Nature* **410**, 259–267 (2001).

**Publisher's note** Springer Nature remains neutral with regard to jurisdictional claims in published maps and institutional affiliations.

© The Author(s), under exclusive licence to Springer Nature Limited 2021

## Methods

### Sample preparation

The multi-component metallic nanoparticle samples were synthesized using thermal shock procedures published elsewhere<sup>44</sup>. Individual metal salts (chlorides or their hydrate forms) were dissolved in ethanol at a concentration of 0.05 mol l<sup>-1</sup>. After complete dissolving with hydrochloric acid, the individual salt precursor solutions with different cations were mixed and sonicated for 30 min. The homogeneously mixed precursor solution was loaded onto carbon substrates<sup>52</sup> (reduced graphene oxide) and heated to a temperature as high as 1,763 K for 55 ms (Extended Data Fig. 1a). The sample was suspended on a trench and connected with copper electrodes by silver paste for both heating and effective cooling. Thermal-shock synthesis was triggered by electric Joule heating in an argon-filled glovebox using a Keithley 2425 SourceMeter in which the high temperature and duration can be effectively controlled by tuning the input power and duration. The temperature of this process was monitored by a high-speed Phantom Miro M110 camera with a pixel size of 25 μm (Supplementary Video 1). The cooling rate was estimated to be  $-5.1-6.9 \times 10^4 \text{ K s}^{-1}$  (Extended Data Fig. 1a), which, according to previous studies, can form metallic glasses<sup>53,54</sup>. The resulting nanoparticles on the reduced graphene oxide were dispersed in ethanol with sonication. After being deposited onto 5-nm-thick silicon nitride membranes, the nanoparticles were baked at 100 °C for 12 h in vacuum to eliminate any hydrocarbon contamination. Both EDX and electron energy loss spectroscopy (EELS) data show that the nanoparticles were still in metallic form and were not oxidized during the experiment (Extended Data Fig. 1b–q).

### Data acquisition

A set of tomographic tilt series was acquired from seven nanoparticles using the TEAM 0.5 microscope with a TEAM stage<sup>55</sup>. Images were collected with an annular dark-field scanning transmission electron microscope (ADF-STEM) operated at 200 kV (Extended Data Table 1). To minimize sample drift, four sequential images per tilt angle were obtained with a dwell time of 3 μs. To monitor any potential damage induced by the electron beam, we took 0° images before, during and after the acquisition of each tilt series and ensured that no noticeable structural change was observed for the seven nanoparticles. The total electron dose of each tilt series was estimated to be between  $7 \times 10^5$  electrons Å<sup>-2</sup> and  $9.5 \times 10^5$  electrons Å<sup>-2</sup> (Extended Data Table 1).

### Image pre-processing and denoising

For each experimental tilt series, we performed the following procedure for image pre-processing and denoising.

(i) Image registration. At each tilt angle, we used the first image as a reference and calculated the normalized cross-correlation between the reference and the other three images using a step size of 0.1 pixel<sup>56</sup>. These four images were aligned and averaged to form an experimental image at that tilt angle.

(ii) Scan distortion correction<sup>39</sup>. Two steps were used to correct the scan distortion for the experimental images. First, a set of low-magnification images of the nanoparticles were taken, and their positions were fitted with a Gaussian. On the basis of the geometric relation of the nanoparticles at different angles, the scan coil directions were calibrated to be perpendicular and equal in strength. Second, six high-magnification images of a multi-component metallic nanoparticle were taken and the scan distortion parameters were estimated by minimizing the mean squared error of the common line of the six images. These scan distortion parameters were applied to the experimental images.

(iii) Image denoising. The experimental images contained mixed Poisson and Gaussian noise, and were denoised by the block-matching and 3D filtering (BM3D) algorithm<sup>57</sup>, which has been demonstrated to be effective in reducing noise in AET<sup>39,41,43</sup>. The BM3D denoising parameters were optimized using the following three steps. First, the Poisson and

Gaussian noise levels were estimated from the experimental tilt series. Second, several images were simulated using a model nanoparticle that has similar size and elemental distribution as an experimental image. The same level of Poisson and Gaussian noise was added to the simulated images. Third, these noisy images were denoised by BM3D with different parameters. The denoising parameters corresponding to the largest cross-correlation coefficient between the denoised and the original images were chosen and applied to denoise the experimental images.

(iv) Background subtraction and alignment. After denoising, a 2D mask slightly larger than the boundary of the nanoparticle was defined from each experimental image. The background inside the mask was estimated using the discrete Laplacian function of MATLAB. After background subtraction, the experimental images of each tilt series were projected onto the tilt axis to produce a set of one-dimensional (1D) curves (termed 'common lines'). The images were aligned along the tilt axis by maximizing the cross-correlation between the common lines. Alignment of the images perpendicular to the tilt axis was achieved by the centre-of-mass method<sup>35</sup>. The centres of mass of the images were calculated and the images were shifted so that all the centres of mass coincided with the origin. This image alignment method has been successfully used to achieve sub-pixel accuracy<sup>35,37,41-43</sup>. The MATLAB data of the raw, processed and aligned experimental images are provided in Supplementary Information.

### The REal Space Iterative REconstruction (RESIRE) algorithm

After pre-processing and denoising, the experimental images were reconstructed using the RESIRE algorithm. The algorithm iteratively minimizes an error function defined by

$$\varepsilon_{\theta}(O) = \frac{1}{2} \sum_{x,y} |\Pi_{\theta}(O)\{x,y\} - b_{\theta}\{x,y\}|^2, \quad (1)$$

where  $\varepsilon_{\theta}(O)$  is an error function of a 3D object ( $O$ ) at tilt angle  $\theta$ ,  $\Pi_{\theta}(O)$  projects  $O$  to generate a 2D image at angle  $\theta$ ,  $b_{\theta}$  is the experimental image at angle  $\theta$  and  $\{x,y\}$  are the coordinates. The minimization is solved via the gradient descent

$$\begin{aligned} \nabla \varepsilon_{\theta}(O)\{u,v,w\} &= \Pi_{\theta}(O)\{x,y\} - b_{\theta}\{x,y\} \\ \text{where } \begin{bmatrix} u \\ v \\ w \end{bmatrix} &= R_{\theta} \begin{bmatrix} x \\ y \\ z \end{bmatrix} \text{ for some } z, \end{aligned} \quad (2)$$

where  $\nabla$  represents the gradient and  $R_{\theta}$  is the rotation matrix at tilt angle  $\theta$ , which transforms coordinates  $\{x,y,z\}$  to  $\{u,v,w\}$ . The  $j$ th iteration of the RESIRE algorithm consists of the following four steps.

(I) A set of images is calculated from the 3D object of the  $j$ th iteration using a Fourier method. The 3D object is first padded with zeros by choosing an appropriate oversampling ratio<sup>58</sup>. Applying the fast Fourier transform to the zero-padded object generates a 3D array in reciprocal space, from which a series of 2D Fourier slices are obtained at different tilt angles. These 2D Fourier slices are inverted to a set of images via the inverse Fourier transform.

(II) The error function defined in equation (1) is calculated using the computed and experimental images.

(III) The gradient of the error function is computed for every voxel using equation (2).

(IV) The 3D object of the  $(j+1)$ th iteration is updated as

$$O^{j+1} = O^j - \frac{\Delta}{nN} \sum_{\theta} \nabla \varepsilon_{\theta}(O^j), \quad (3)$$

where  $\Delta$  is the step size ( $\Delta = 2$  was chosen for the reconstruction of our experimental data),  $n$  is the number of images and  $N$  is the dimension of each image ( $N \times N$ ).  $O^{j+1}\{u,v,w\}$  is used as input for the  $(j+1)$ th iteration.

The convergence of the algorithm is monitored by the  $R$  factor

$$R = \frac{1}{n} \sum_{\theta} \frac{\sum_{x,y} |\Pi_{\theta}(O)\{x,y\} - b_{\theta}\{x,y\}|}{\sum_{x,y} |b_{\theta}\{x,y\}|} \quad (4)$$

Usually, after several hundreds of iterations, the algorithm converges to a high-quality 3D reconstruction from a limited number of images. Both our numerical simulation and experimental results have indicated that RESIRE outperforms other iterative tomographic algorithms such as generalized Fourier iterative reconstruction<sup>59</sup> and the simultaneous iterative reconstruction technique<sup>60</sup>. By avoiding iterating between real and reciprocal space, RESIRE can be applied to general sample geometries such as thin films and extended objects. The details of the RESIRE algorithm will be reported in a follow-up paper.

For each aligned experimental tilt series, we first ran RESIRE for 200 iterations. From the initial 3D reconstruction, we performed the angular refinement and spatial alignment for the experimental images<sup>41,59</sup>. For each experimental image, we determined the corresponding three Euler angles of the 3D reconstruction. We sequentially scanned each of the three Euler angles with a small angular increment. At each scanning step, we projected back the 3D reconstruction to obtain an image. The experimental image was shifted along the  $x$  and  $y$  axes and aligned with the calculated one. An error metric, defined as the difference between the calculated and experimental image, was computed. After scanning all three Euler angles, the three optimal Euler angles with the smallest error metric were found. This procedure was iterated for all the experimental images until there was no further improvement, producing a set of spatially aligned experimental images and refined tilt angles. Next, the background of each experimental image was re-evaluated and re-subtracted. Using these experimental images with the refined tilt angles (Extended Data Fig. 4a), we ran another 200 iterations of RESIRE to obtain the final 3D reconstruction of each experimental tilt series (Extended Data Table 1). The source codes of RESIRE are provided in Supplementary Information.

## Determination of 3D atomic coordinates and species

From each final 3D reconstruction, the atomic coordinates and species were identified using the following procedure<sup>41,43</sup>.

(a) Each 3D reconstruction was upsampled by a factor of 3 using the spline interpolation, from which all the local maxima were identified. Starting from the highest intensity peak, polynomial fitting<sup>61</sup> was performed on a  $0.8 \times 0.8 \times 0.8 \text{ \AA}^3$  ( $7 \times 7 \times 7$  voxel) volume around each local maximum to locate the peak position. If the distance between the fitted peak position and existing potential atom positions was larger than or equal to  $2 \text{ \AA}$ , it was listed as a potential atom. After repeating this step for all the local maxima, a list of potential atom positions was obtained. This method of tracing the positions of potential atoms has previously been rigorously tested by using two independent experimental tilt series acquired from the same sample<sup>43</sup>.

(b) A 3D difference map was generated by taking the difference between the 3D reconstruction and the list of the potential atoms. Based on the difference map, we manually adjusted a very small fraction of the atoms (167 out of 18,356), which has been routinely used in protein crystallography<sup>62</sup>.

(c) A K-mean clustering method<sup>41,43,63</sup> was used to classify three types of atom and non-atom (Co and Ni as type 1; Ru, Rh, Pd and Ag as type 2; and Ir and Pt as type 3) on the basis of the integrated intensity of a  $0.8 \times 0.8 \times 0.8 \text{ \AA}^3$  volume around each potential atom position. An initial atomic model with 3D atomic coordinates was determined from each 3D reconstruction.

(d) Owing to the missing wedge problem and the noise in the experimental images, there was local intensity variation in each 3D reconstruction. A local reclassification was iteratively performed to refine the type-1, -2 and -3 atoms. Each atom was defined as the centre of a  $10\text{-\AA}$ -radius sphere. The average intensity distribution of type-1, -2 and

-3 atoms was computed within the sphere. The  $L_2$  norm of the intensity distribution between the centre atom and the average type-1, -2 and -3 atom was calculated. The centre atom was assigned to the type with the smallest  $L_2$  norm. The procedure was iteratively repeated until there were no further changes. The source codes for the 3D atom tracing and classification are provided in Supplementary Information.

## Refinement of 3D atomic coordinates

The 3D atomic coordinates were refined by minimizing the error between the calculated and measured images using the gradient descent<sup>39,41,43</sup>. Each atom was first fitted with a 3D Gaussian function with height  $H$  and width  $B'$ , where  $H$  and  $B'$  were considered to be the same for the same type of atom. A 3D atomic model was obtained by

$$O\{x,y,z\} = \sum_i H_i \exp\left(-\frac{|x-x_i|^2 + |y-y_i|^2 + |z-z_i|^2}{B_i'}\right), \quad (5)$$

where  $x_i, y_i, z_i, H_i$  and  $B_i'$  are the coordinates, height and standard deviation of the  $i$ th atom, respectively, and  $|x-x_i|, |y-y_i|, |z-z_i| \leq \rho$ , where  $\rho$  is the cut-off size of the 3D Gaussian function. From the 3D atomic model, a set of projection images were computed at different tilt angles  $\theta$  by

$$\Pi_{\theta}(O)\{u,v\} = \sum_w \sum_i H_i \exp\left(-\frac{|u-u_i|^2 + |v-v_i|^2 + |w-w_i|^2}{B_i'}\right) \quad (6)$$

where  $\begin{bmatrix} u_i \\ v_i \\ w_i \end{bmatrix} = R_{\theta} \begin{bmatrix} x_i \\ y_i \\ z_i \end{bmatrix}$  and  $|u-u_i|, |v-v_i|, |w-w_i| \leq \rho$ .

By substituting equation (6) into equation (1), an error function was calculated, from which the optimal atomic position at the  $(j+1)$ th iteration was obtained using the gradient descent method

$$\{x_i, y_i, z_i\}^{j+1} = \{x_i, y_i, z_i\}^j - \Delta \sum_{\theta} [\Pi_{\theta}(O)\{u,v\} - b_{\theta}\{u,v\}] \nabla_i [\Pi_{\theta}(O)\{u,v\}], \quad (7)$$

where  $\nabla_i$  is the spatial gradient operator with respect to the atomic position  $(x_i, y_i, z_i)$ . The iterative refinement process was terminated when the  $L_2$  norm error could not be further reduced.

## 3D precision estimation with multi-slice simulations

A tilt series of 55 STEM images was generated from the experimental 3D atomic model using fast multi-slice simulation software based on a graphics processing unit<sup>64</sup>. At each refined experimental angle (Extended Data Fig. 4a), the experimental 3D atomic model was placed in a cuboidal supercell and the supercell was divided into multiple  $2\text{-\AA}$ -thick slices along the  $z$  axis. The experiment parameters shown in Extended Data Table 1 (particle 1) were used for the multi-slice simulations. After using parallel computing to perform the multi-slice simulations for all angles, we generated 55 multi-slice STEM images, each with  $289 \times 289$  pixels and a pixel size of  $0.347 \text{ \AA}$ . To account for the electron probe size and other incoherent effects, each multi-slice STEM image was convolved with a Gaussian kernel. Extended Data Fig. 4c, d shows representative experimental and multi-slice STEM images. The average  $R$  factor for the 55 experimental and multi-slice images (defined in equation (4)) was computed to be 14.96%, which, according to the crystallography standard<sup>62</sup>, represents good agreement between the two sets of images.

From the 55 multi-slice STEM images with angular errors (Extended Data Fig. 4a), we performed the 3D reconstruction and angular refinement with RESIRE (Extended Data Fig. 4b). After applying the atomic tracing, classification and refinement procedure to the reconstruction, we obtained a new 3D atomic model of the sample, consisting of 8,438, 6,905 and 3,138 type-1, -2 and -3 atoms, respectively. We identified 7,898, 6,837 and 3,138 common pairs of type-1, -2 and -3 atoms, respectively,

between the experimental and multi-slice atomic models according to the criterion of each common pair having a radius within 1.5 Å. The total number of common pairs for the three types of atom are 17,873, indicating that 97.37% of all atoms have been correctly identified. Extended Data Fig. 4d shows the distribution of the atomic deviation between all the common pairs with a root-mean-square deviation (that is, 3D precision) of 21 pm.

### The local BOO parameters

The local BOO parameters ( $Q_4$  and  $Q_6$ ) were calculated from the 3D atomic model of each nanoparticle using a method described elsewhere<sup>65,66</sup>. The  $Q_4$  and  $Q_6$  order parameters were computed up to the second shell with a shell radius set by the first valley in the PDF curve of the 3D atomic model (Fig. 1g). Figure 1f and Extended Data Fig. 2h–n show the distribution of the local BOO parameters for all the atoms in particles 1–7. To separate the amorphous structure from the crystal nuclei, we calculated the normalized BOO parameter, defined as  $\sqrt{Q_4^2 + Q_6^2} / \sqrt{Q_{4fcc}^2 + Q_{6fcc}^2}$  where  $Q_{4fcc}$  and  $Q_{6fcc}$  are the  $Q_4$  and  $Q_6$  values, respectively, for a perfect fcc lattice. The normalized BOO parameter is between 0 and 1, where 0 means that  $Q_4 = Q_6 = 0$  and 1 represents a perfect fcc crystal structure. On the basis of the BOO parameters of a  $\text{Cu}_{65}\text{Zr}_{35}$  metallic-glass structure obtained from molecular dynamics simulations<sup>67</sup> (Extended Data Fig. 2o), we chose the normalized BOO parameter of 0.5 as a cut-off to separate crystal nuclei from amorphous structure (red curves in Fig. 1f and Extended Data Fig. 2h–n).

### Characterization of the crystalline–amorphous interface

The 3D surface of each crystal nucleus was defined by setting the normalized BOO parameter at  $\geq 0.5$ . For every atom, the perpendicular distance to the 3D surface of its closest crystal nucleus was calculated. If the atom was inside the nucleus, the distance was considered negative, otherwise it was positive. After counting all the atoms in the nanoparticle, a 1D curve was created to represent the normalized BOO parameter as a function of the distance. An exponential decay function  $y = ae^{-x/d_c} + b$  was used to fit the 1D curve, where  $a$  and  $b$  are constants and  $d_c$  is the characteristic width of the crystalline–amorphous interface. For the crystal nuclei in the glass-forming nanoparticle,  $d_c$  was determined to be 3.69 Å, which is consistent with the molecular dynamics simulation of a poor glass former<sup>31</sup>.

### PDF and partial PDF

The PDF was calculated for the 3D atomic model of each nanoparticle using the following procedure. (1) The distance of all atom pairs in each 3D atomic model was computed and binned into a histogram. (2) The number of atom pairs in each bin was normalized with respect to the volume of the spherical shell corresponding to each bin. (3) The histogram was scaled so that the PDF approached 1 for large separations. After plotting the PDF for each nanoparticle, the first valley of the PDF was used as the nearest-neighbour cut-off distance to calculate the local BOO parameters (Fig. 1f, Extended Data Fig. 2h–n). By choosing atoms in the glass-forming nanoparticle with normalized BOO parameter  $< 0.5$ , we applied the above procedure to plot the PDF (Fig. 1g). For type-1, -2 and -3 atoms, we identified six sets of atom pairs (type 11, 12, 13, 22, 23 and 33) in the nanoparticle. For each set of atom pairs, we used the above procedure to calculate the partial PDF shown in Fig. 1h.

### Voronoi tessellation and the coordination number

The analysis of the Voronoi tessellation was performed by following a procedure published elsewhere<sup>8</sup>, in which the surface atoms of the nanoparticle were excluded. To reduce the effect of the experimental and reconstruction error on the Voronoi tessellation, surfaces with areas of less than 1% of the total surface area of each Voronoi polyhedron were removed<sup>11</sup>. From the Voronoi tessellation, each polyhedron was

designated a Voronoi index  $n_1, n_2, \dots$  with  $n_i$  denoting the number of  $i$ -edged faces, and the coordination number was calculated from  $\sum_i n_i$ .

To examine the effect of the 3D precision of AET on the Voronoi tessellation, we used a  $\text{Cu}_{65}\text{Zr}_{35}$  metallic-glass structure obtained from molecular dynamics simulations<sup>67</sup>. A 3D atomic model was cropped from the structure to have the similar 3D shape and size to the experimental nanoparticle (particle 1). Our Voronoi analysis reveals that the ten most abundant Voronoi polyhedra in the atomic model are  $\langle 0, 0, 12, 0 \rangle$ ,  $\langle 0, 2, 8, 2 \rangle$ ,  $\langle 0, 2, 8, 1 \rangle$ ,  $\langle 0, 1, 10, 2 \rangle$ ,  $\langle 0, 3, 6, 4 \rangle$ ,  $\langle 0, 3, 6, 3 \rangle$ ,  $\langle 0, 1, 10, 4 \rangle$ ,  $\langle 0, 2, 8, 4 \rangle$ ,  $\langle 0, 1, 10, 3 \rangle$  and  $\langle 0, 0, 12, 3 \rangle$ . Their corresponding fractions are 14.26%, 10.26%, 7.97%, 6.92, 4.58%, 4.14%, 4.01%, 3.41%, 2.97% and 2.32%, respectively. After adding the experimental error (Extended Data Fig. 4e) to the atomic model, the corresponding fractions of these ten Voronoi polyhedra become 13.70%, 9.95%, 7.91%, 6.97%, 4.63%, 4.08%, 3.57%, 3.42%, 2.89% and 2.19%, respectively. This analysis indicates that the 3D precision of AET has only a small effect on the Voronoi tessellation.

### Quantification of the chemical SRO

We used the Warren–Cowley parameters ( $\alpha_{lm}$ ) to quantify the chemical SRO<sup>68,69</sup>

$$\alpha_{lm} = 1 - \frac{Z_{lm}}{\chi_m Z_l}, \quad (8)$$

where  $l, m = 1, 2$  or 3,  $Z_{lm}$  is the partial coordination number of type- $m$  atoms around type- $l$  atoms,  $\chi_m$  is the fraction of type- $m$  atoms and  $Z_l$  is the total coordination number around type- $l$  atoms. After excluding the surface atoms, we estimated  $\chi_1, \chi_2$  and  $\chi_3$  to be 42.97%, 38.28% and 18.75%, respectively. Using the partial coordination numbers (Extended Data Fig. 5b), we calculated  $\alpha_{11} = -0.11$ ,  $\alpha_{12} = 0.1$ ,  $\alpha_{13} = 0.05$ ,  $\alpha_{21} = 0.02$ ,  $\alpha_{22} = 0.01$ ,  $\alpha_{23} = -0.07$ ,  $\alpha_{31} = 0.03$ ,  $\alpha_{32} = -0.06$  and  $\alpha_{33} = 0.06$ , indicating that type-11 and -23 bonds are favoured but type-12 and -33 bonds are disfavoured. These results are consistent with the observations that the type-23 bond is 0.06 Å shorter than the average type-2 and -3 bonds and the type-12 bond is 0.06 Å longer than the average type-1 and -2 bonds (Fig. 1h).

### Determination of solute centres and MROs

A breadth-first search algorithm<sup>70,71</sup> was implemented to search for the solute centres and MROs using the following procedure. First, the algorithm identified the solute centres from type-3 atoms based on two criteria: (i) each solute centre must fall within a 0.75 Å radius from an fcc, hcp, bcc or sc lattice point, and (ii) each solute centre must have at least one neighbouring type-3 atom within the second-coordination-shell distance. Second, the identified solute centres were sorted out to generate a queue of the fcc-, hcp-, bcc- or sc-like MRO candidates. Third, starting from the largest MRO candidate (that is, with the most solute centres), each candidate was classified as an MRO if it had at least five or more solute centres and none of the solute centres was already occupied by another MRO. If any solute centres were already occupied, they were removed from the MRO candidate, and the candidate was refitted into the lattice vectors and added back into the queue. If two or more MRO candidates had the same number of solute centres, the one with the smallest error of fitting the solute centres into the lattice vectors was analysed first. This process was repeated until all the MROs were identified, in which each solute centre could only belong to no more than one MRO. To corroborate our analysis, we repeated the above steps with 1-Å and 0.5-Å radius cut-offs, and the corresponding MROs are shown in Extended Data Figs. 6, 7, respectively.

An attempt was also made to search for icosahedral-like MROs. The breadth-first search algorithm<sup>70,71</sup> was used to find the MROs that fall within a 0.75 Å radius from the 12 vertices of an icosahedron. Because the icosahedron cannot be periodically packed in three dimensions, only the nearest-neighbour vertices were searched, making the largest possible MRO have 13 solute centres (one central solute centre plus

# Article

12 nearest neighbours). After performing the search, the resulting possible MROs had a mean value of 3.9, meaning that on average each solute centre was connected to only three others when constrained to an icosahedron within the second coordination shell. Furthermore, although the largest possible MRO had seven solute centres, none of these solute centres formed five-fold symmetry. We also repeated this analysis with a 1-Å radius cut-off; the mean value of solute centres became 4.5, the largest MRO had eight solute centres, and there were 19 five-fold symmetries. The source codes used to identify the MROs are provided in Supplementary Information.

## Determination of the 3D atomic structure of an amorphous CuTa thin film

The following procedure was used to experimentally resolve the 3D atomic positions in the CuTa thin film.

(i) Sample preparation. CuTa thin films were fabricated in situ in the sample chamber of the spin-polarized low-energy electron microscope at the National Center for Electron Microscopy at Berkeley, USA, where clean ultrahigh-vacuum conditions remained in the low  $10^{-9}$  torr range. Using thermal evaporation, CuTa thin films were deposited on  $\text{Si}_3\text{N}_4$  substrates, which were maintained at well below 150 K during sample fabrication. The growth rate of the thin films was in the range of 0.1–1 atomic monolayers per minute. After the fabrication of the CuTa thin films, a very thin carbon capping layer was deposited on the films to protect the samples from oxidation.

(ii) Data acquisition. A tomographic tilt series was acquired from the CuTa thin film using the TEAM I microscope in ADF-STEM mode at 300 kV. To mitigate the sample drift, two images were taken at each tilt angle and then aligned to improve the signal-to-noise ratio. The tilt series consists of a total of 40 images with a tilt ranging from  $-67.9^\circ$  to  $64.9^\circ$  (Extended Data Fig. 8). Because the CuTa film is thinner than  $\sim 6$  nm, 40 experimental images are sufficient to produce a good 3D reconstruction. The total electron dose of the dataset is  $2.4 \times 10^5$  electrons  $\text{\AA}^{-2}$ . The experimental parameters of the tilt series are shown in Extended Data Table 1.

(iii) Image alignment. The image pre-processing and denoising steps for the analysis of the CuTa thin film are similar to those used for the glass-forming nanoparticle, except for image alignment. We first used the cross-correlation between the neighbouring images to roughly align the CuTa images. Next, we searched for some reference markers, which can be either created by adding some small nanoparticles or based on features in the sample. In this experiment, we chose an isolated region in the images and aligned them using the centre-of-mass and common-line method<sup>35,37</sup>. After obtaining the 3D reconstruction, we further refined the alignment by projecting back the reconstruction to generate images and comparing them with the experimental ones. This process was repeated until no further improvement could be made.

(iv) 3D reconstruction, atomic tracing and refinement. Using RESIRE, we first performed a large volume reconstruction of the CuTa thin film from the aligned images. On the basis of the thickness variation of the thin film, we applied scanning AET<sup>42</sup> to conduct multiple local volume reconstructions and then patched them together to produce a full 3D reconstruction. Scanning AET has been previously demonstrated to be effective in improving the 3D reconstruction of 2D materials and/or thin-film samples<sup>42</sup>. Using the full 3D reconstruction, we projected it back to generate images and used them to perform angular refinement and spatial alignment. We iteratively repeated the process until there were no further changes. After obtaining the final 3D reconstruction, we traced the Cu and Ta atoms using the integrated intensity difference between the two types of atom. The 3D atomic positions were refined to produce a final 3D atomic model of the CuTa thin film (Extended Data Fig. 9).

## Data availability

The raw and processed experimental data are available at <https://github.com/AET-MetallicGlass/Supplementary-Data-Codes>. The 3D atomic

coordinates of the glass-forming nanoparticle have been deposited in the Materials Data Bank ([www.materialsdatbank.org](http://www.materialsdatbank.org)) with MDB ID NiRh00001.

## Code availability

The MATLAB source codes for the RESIRE reconstruction and data analysis used in this work are available at <https://github.com/AET-MetallicGlass/Supplementary-Data-Codes>.

- Xu, Z., Sun, H., Zhao, X. & Gao, C. Ultrastrong fibers assembled from giant graphene oxide sheets. *Adv. Mater.* **25**, 188–193 (2013).
- Takeuchi, A. & Inoue, A. Quantitative evaluation of critical cooling rate for metallic glasses. *Mater. Sci. Eng. A* **304–306**, 446–451 (2001).
- Bordeenthikasem, P. et al. Determination of critical cooling rates in metallic glass forming alloy libraries through laser spike annealing. *Sci. Rep.* **7**, 1755 (2017); author correction **8**, 17898 (2018).
- Ercius, P., Boese, M., Duden, T. & Dahmen, U. Operation of TEAM I in a user environment at NCEM. *Microsc. Microanal.* **18**, 676–683 (2012).
- Lewis, J. P. Fast normalized cross-correlation. In *Vision Interface 1995* 120–123 (1995).
- Dabov, K., Foi, A., Katkovnik, V. & Egiazarian, K. Image denoising by sparse 3-D transform-domain collaborative filtering. *IEEE Trans. Image Process.* **16**, 2080–2095 (2007).
- Miao, J., Sayre, D. & Chapman, H. N. Phase retrieval from the magnitude of the Fourier transform of non-periodic objects. *J. Opt. Soc. Am. A* **15**, 1662–1669 (1998).
- Pryor, A. et al. GENFIRE: a generalized Fourier iterative reconstruction algorithm for high-resolution 3D imaging. *Sci. Rep.* **7**, 10409 (2017).
- Gilbert, P. Iterative methods for the three-dimensional reconstruction of an object from projections. *J. Theor. Biol.* **36**, 105–117 (1972).
- Rogers, S. S., Waigh, T. A., Zhao, X. & Lu, J. R. Precise particle tracking against a complicated background: polynomial fitting with Gaussian weight. *Phys. Biol.* **4**, 220–227 (2007).
- Brünger, A. T. et al. Crystallography & NMR System: a new software suite for macromolecular structure determination. *Acta Crystallogr. D* **54**, 905–921 (1998).
- Lloyd, S. Least squares quantization in PCM. *IEEE Trans. Inf. Theory* **28**, 129–137 (1982).
- Pryor, A., Ophus, C. & Miao, J. A streaming multi-GPU implementation of image simulation algorithms for scanning transmission electron microscopy. *Adv. Struct. Chem. Imaging* **3**, 15 (2017).
- Steinhardt, P. J., Nelson, D. R. & Ronchetti, M. Bond-orientational order in liquids and glasses. *Phys. Rev. B* **28**, 784–805 (1983).
- Lechner, W. & Dellago, C. Accurate determination of crystal structures based on averaged local bond order parameters. *J. Chem. Phys.* **129**, 114707 (2008).
- Yu, H. B. & Samwer, K. Atomic mechanism of internal friction in a model metallic glass. *Phys. Rev. B* **90**, 144201 (2014).
- Warren, B. E. *X-Ray Diffraction* (Dover Publications, 1990).
- Cowley, J. M. X-Ray measurement of order in single crystals of  $\text{Cu}_3\text{Au}$ . *J. Appl. Phys.* **21**, 24–30 (1950).
- Lee, C. Y. An algorithm for path connections and its applications. *IEEE Trans. Electron. Comput.* **EC-10**, 346–365 (1961).
- Larsen, P. M., Schmidt, S. & Schiötz, J. Robust structural identification via polyhedral template matching. *Model. Simul. Mater. Sci. Eng.* **24**, 055007 (2016).

**Acknowledgements** We thank J. Ding for discussions, H. B. Yu for providing a molecular-dynamics-simulated atomic model of the  $\text{Cu}_{62}\text{Zr}_{38}$  metallic glass, and D. J. Kline and M. R. Zachariah for assistance with the temperature measurements. This work was primarily supported by STROBE: A National Science Foundation Science & Technology Center under grant number DMR 1548924. This work was also supported by the US Department of Energy (DOE), Office of Science, Basic Energy Sciences, Division of Materials Sciences and Engineering under award number DE-SC0010378 (data acquisition and 3D image reconstruction) and the NSF DMREF programme under award number DMR-1437263. J.M. acknowledges partial support from an Army Research Office MURI grant on Ab-Initio Solid-State Quantum Materials: Design, Production and Characterization at the Atomic Scale. Y. Yao and L.H. are supported by the National Science Foundation (award number 1635221). The ADF-STEM imaging with TEAM 0.5 was performed at the Molecular Foundry, which is supported by the Office of Science, Office of Basic Energy Sciences of the US DOE under contract number DE-AC02–05CH11231.

**Author contributions** J.M. conceived the idea and directed the project; Y. Yao and L.H. synthesized the samples; J.Z., P.E., A.K.S. and J.M. discussed and/or carried out the experiments; M.P., Y. Yuan, A.R., S.J.O. and J.M. developed the RESIRE algorithm. Y. Yang, F.Z., Y. Yuan, D.J.C., J.Z., D.S.K., X.T. and J.M. performed image reconstruction, atom tracing and classification, analysed the data and/or interpreted the results; J.M., Y. Yang, J.Z. and F.Z. wrote the manuscript. All authors commented on the manuscript.

**Competing interests** The authors declare no competing interests.

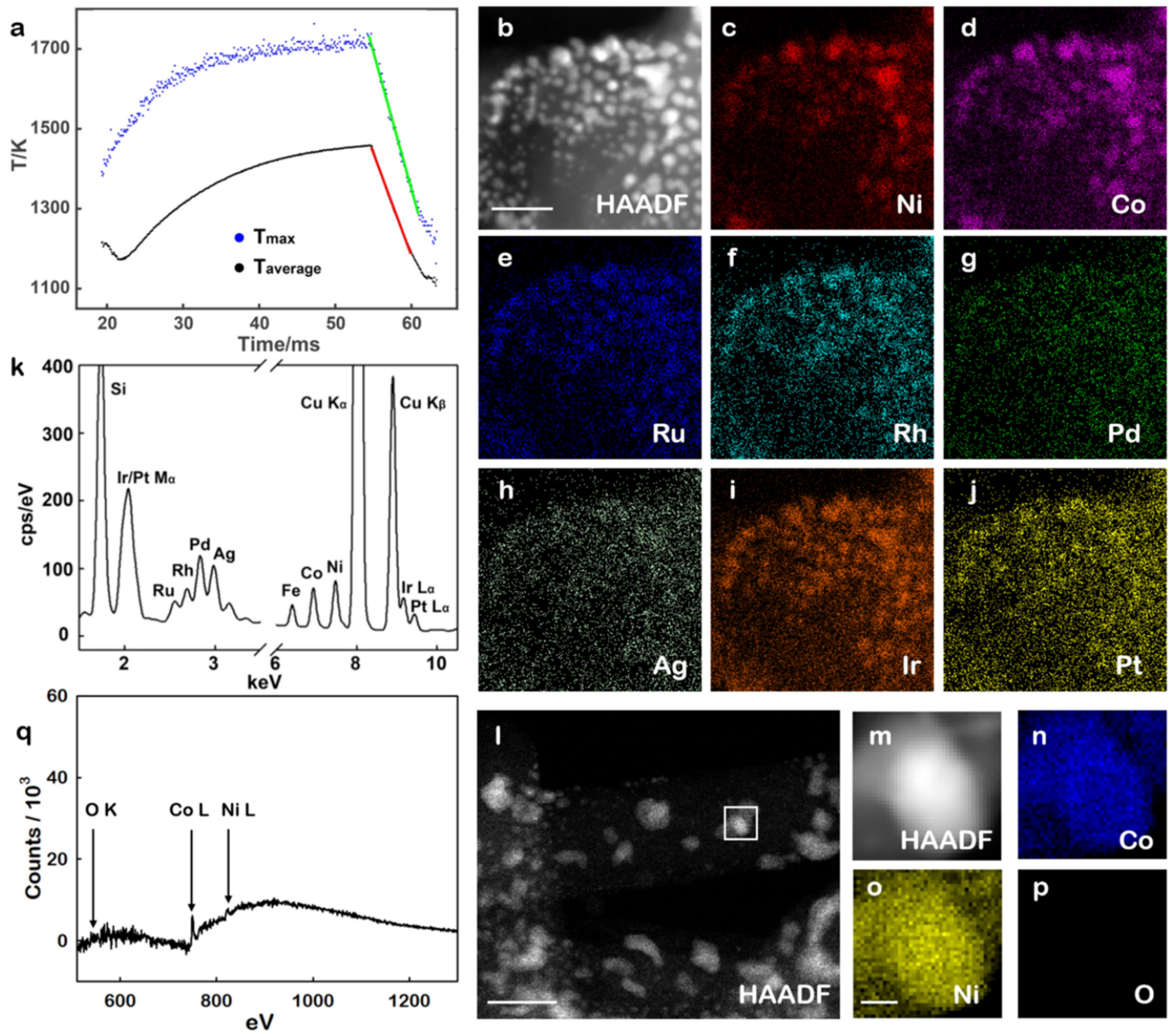
## Additional information

**Supplementary information** The online version contains supplementary material available at <https://doi.org/10.1038/s41586-021-03354-0>.

**Correspondence and requests for materials** should be addressed to J.M.

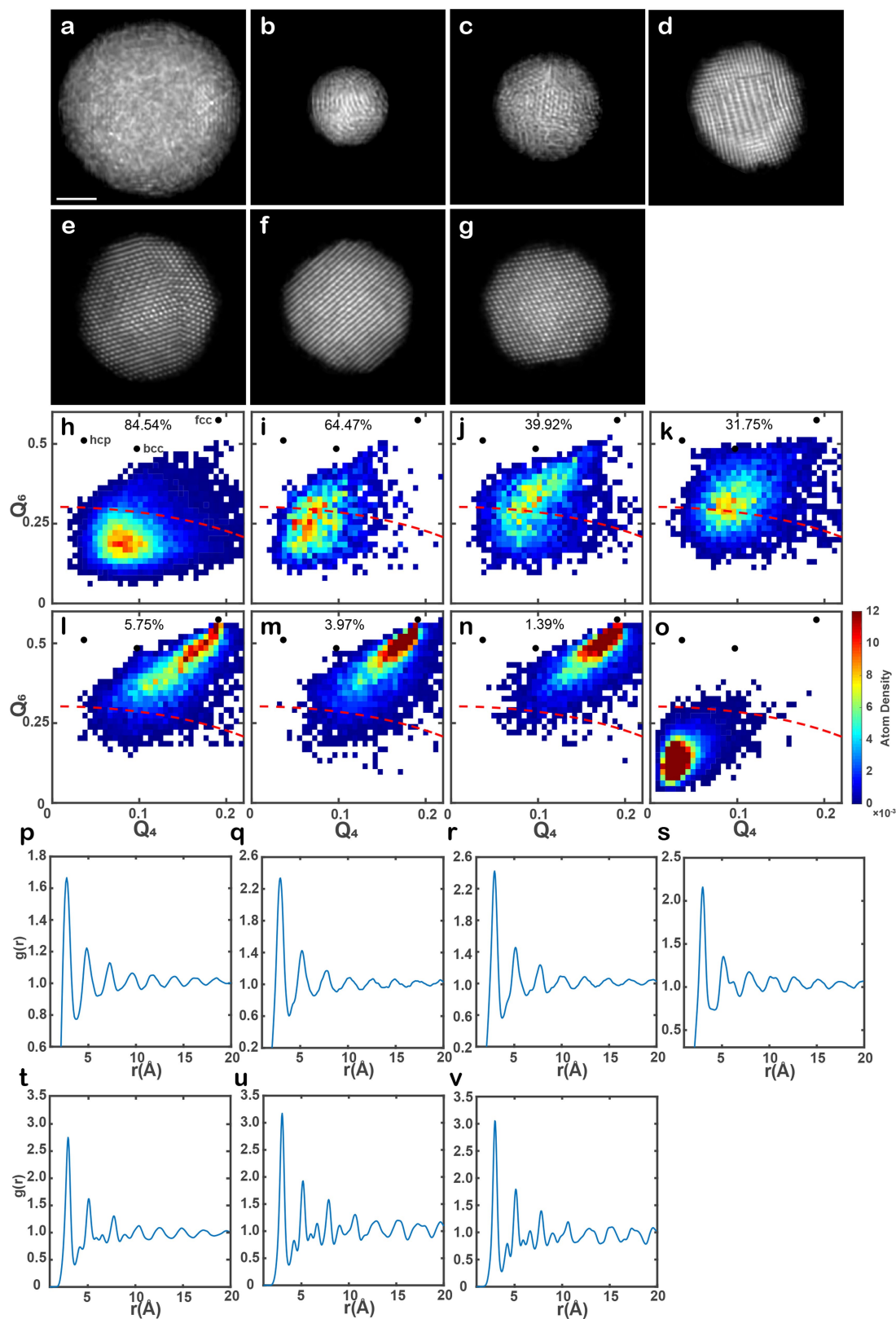
**Peer review information** *Nature* thanks Simon Billinge, Paul Voyles, Yong Yang and the other, anonymous, reviewer(s) for their contribution to the peer review of this work. Peer reviewer reports are available.

**Reprints and permissions information** is available at <http://www.nature.com/reprints>.



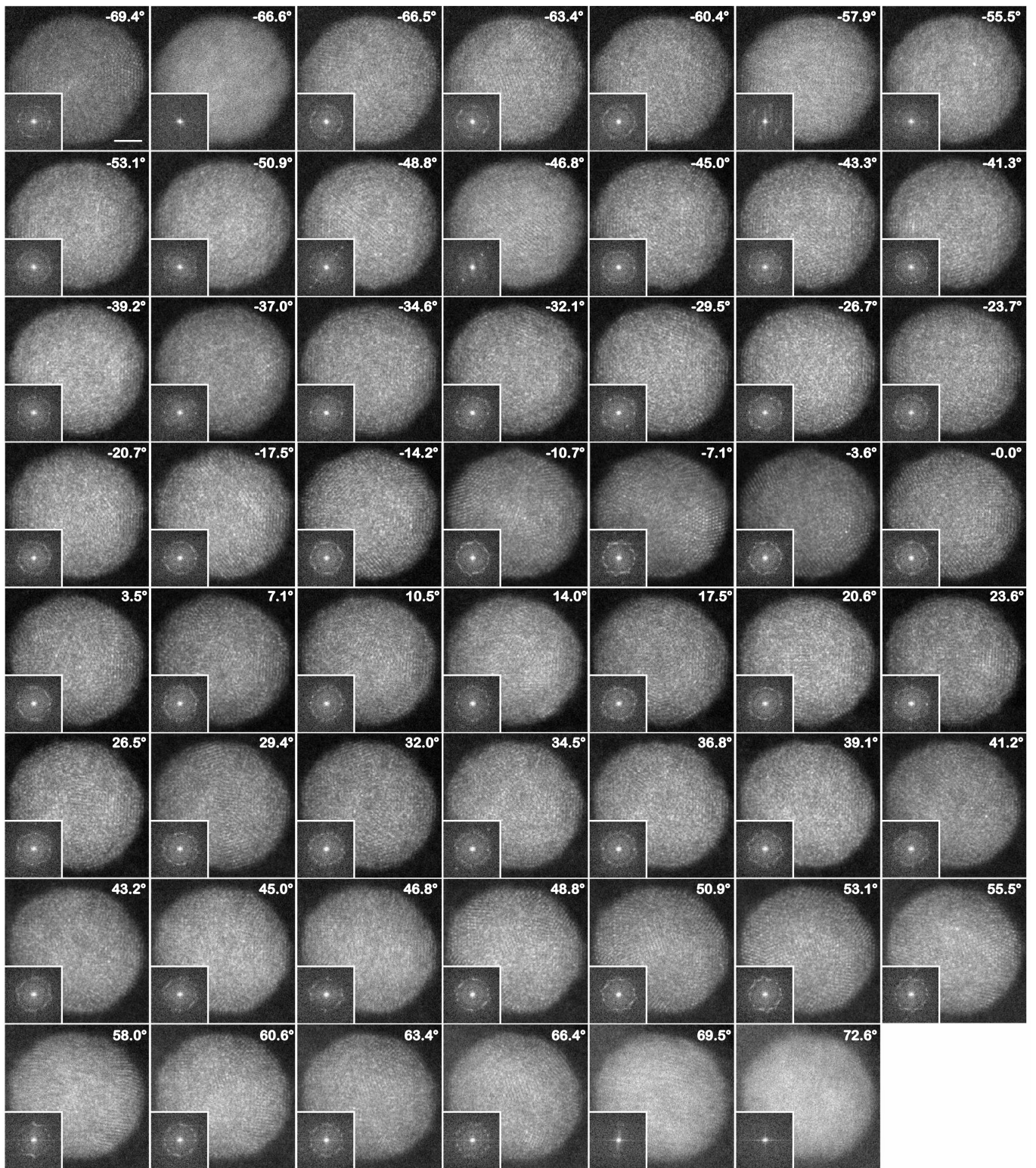
**Extended Data Fig. 1 | Cooling rate measurement, EDX and EELS maps of the nanoparticles.** **a**, The cooling rate for the average ( $T_{average}$ ) and maximum ( $T_{max}$ ) temperature curves was measured to be  $51,000 \text{ K s}^{-1}$  (slope of the red line) and  $69,000 \text{ K s}^{-1}$  (slope of the green line), respectively. **b**, Low-resolution ADF-STEM image of the nanoparticles. **c–j**, EDX maps showing the distribution of Ni (**c**), Co (**d**), Ru (**e**), Rh (**f**), Pd (**g**), Ag (**h**), Ir (**i**) and Pt (**j**). **k**, EDX spectrum of all the elements shown in **c–j**; cps, counts per second. **l**, Low-resolution ADF-STEM

image of a large area, with the white square indicating the aggregation of several nanoparticles used for the EELS measurement. **m**, ADF-STEM image of the region in the white square in **l**. **n–p**, EELS maps show the distribution of Co (**n**), Ni (**o**) and O (**p**) in the same region. **q**, EELS spectrum obtained from **n–p**. No oxygen signal was detected in the EELS map or spectrum. Scale bars, 20 nm (**b**); 100 nm (**l**); and 10 nm (**o**).



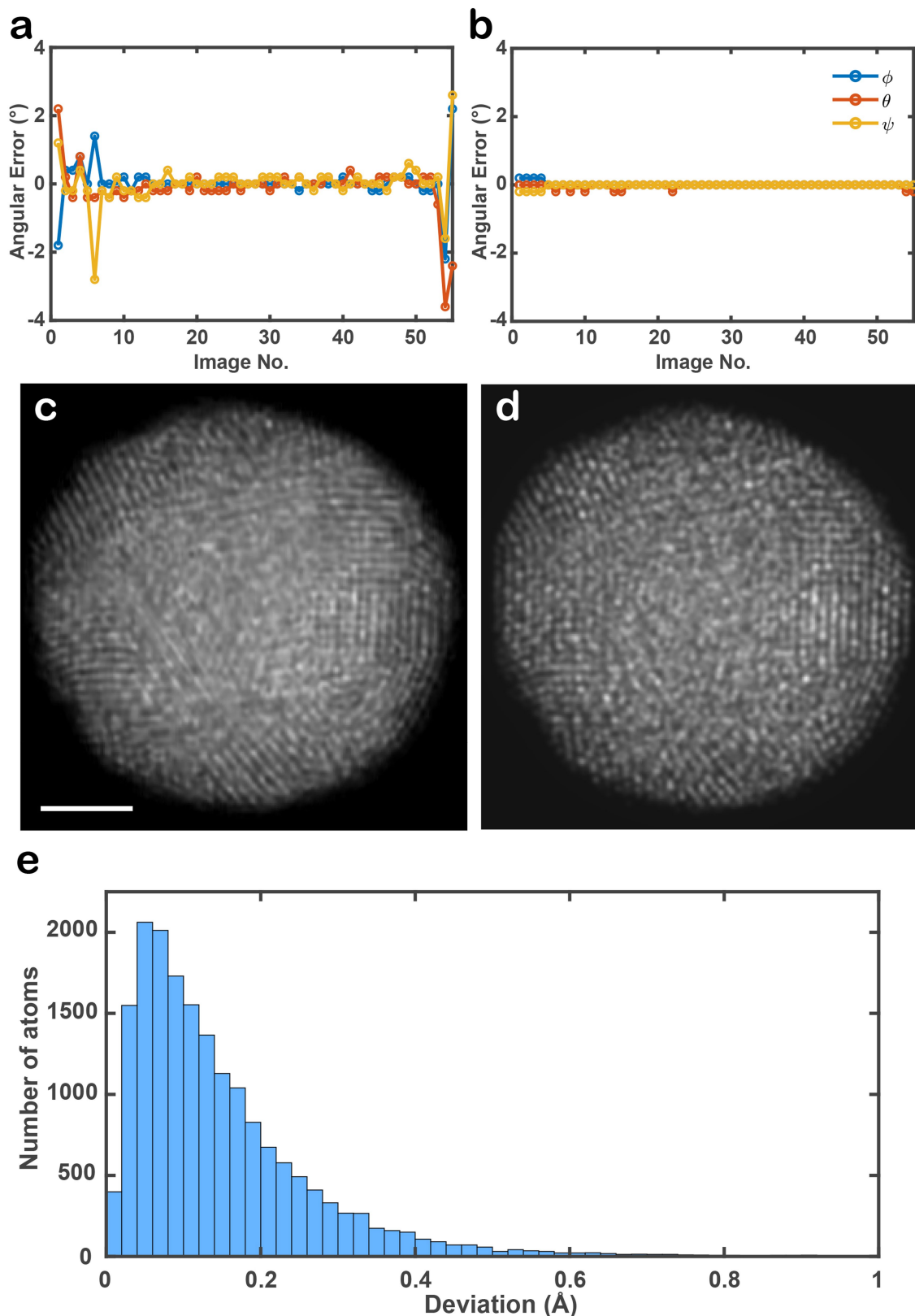
**Extended Data Fig. 2 | Analysis of seven multi-component metallic nanoparticles.** **a–g**, Representative ADF-STEM images of particles 1–7, respectively. Scale bar, 2 nm. **h–n**, Local BOO parameters for all atoms in particles 1–7, where the dashed red curves correspond to a normalized BOO parameter of 0.5. The percentage at the top of each panel shows the fraction of disordered atoms in each particle. **o**, Local BOO parameters of a 3D atomic model cropped from a molecular-dynamics-simulated  $\text{Cu}_{65}\text{Zr}_{35}$  metallic glass<sup>67</sup>

used as a reference, from which a normalized BOO parameter of 0.5 (dashed red curve) was chosen as a cut-off to separate crystal nuclei from amorphous structure. For a fair comparison, the 3D atomic model was cropped to have a similar 3D shape and size to the experimental nanoparticle (particle 1). **p–v**, PDFs of all atoms in particles 1–7, respectively. With decreasing fraction of disordered atoms in the nanoparticles, the peaks in the PDFs become narrower and new peaks corresponding to different crystal planes appear.



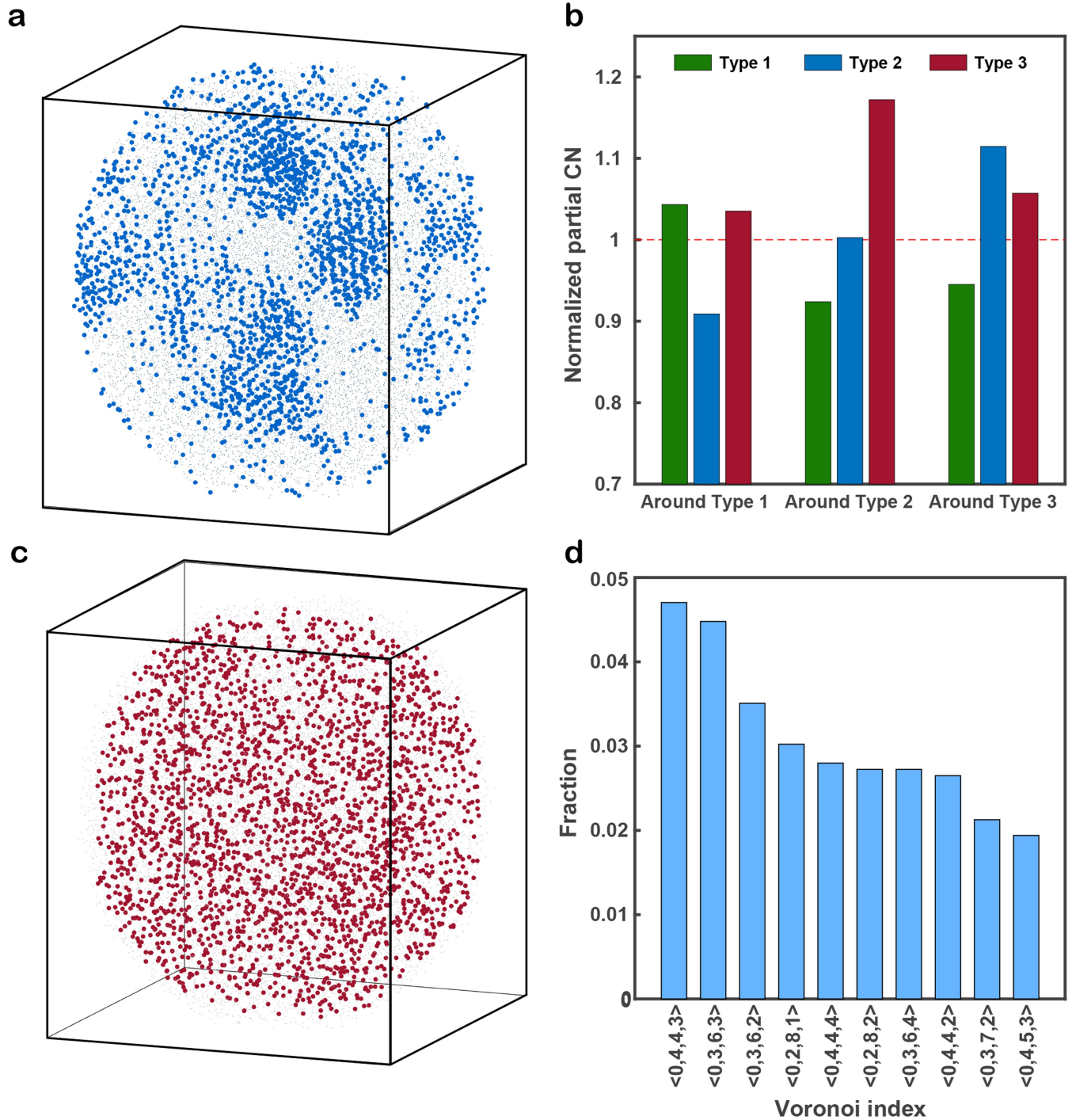
**Extended Data Fig. 3 | Experimental tomographic tilt series of a multi-component glass-forming nanoparticle (particle 1).** 55 raw ADF-STEM images of the nanoparticle with a tilt range from  $-69.4^\circ$  to  $+72.6^\circ$ . The 2D power

spectra of the images are shown in the insets, where the amorphous halo is visible. Some crystalline features are visible in several experimental images and the 2D power spectra. Scale bar, 2 nm.



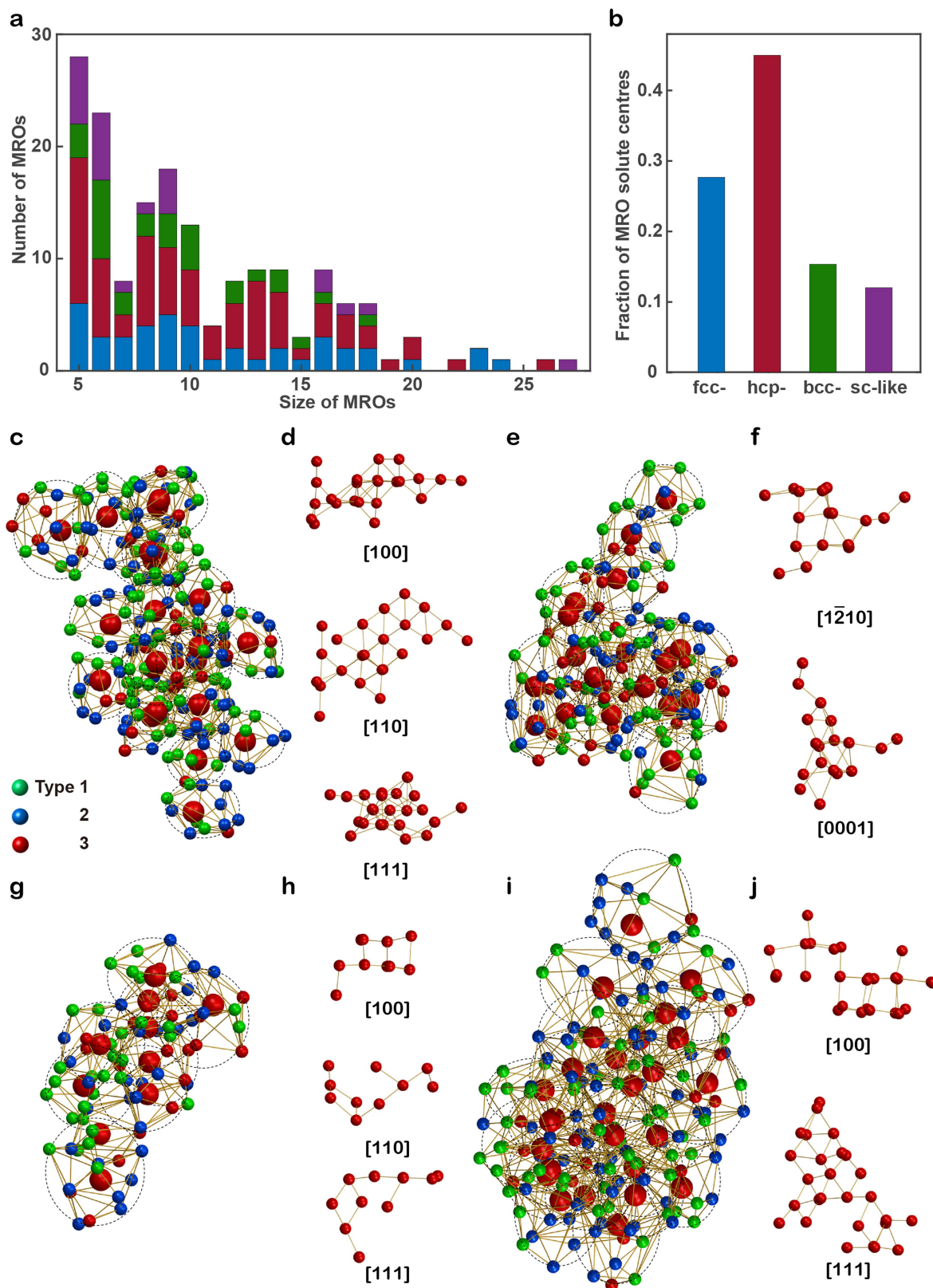
**Extended Data Fig. 4 | Angular errors in the experimental images and verification of the experimental 3D atomic model using multi-slice simulations.** **a**, Angular errors in the experimental images determined by an angular refinement procedure (Methods), where the colour dots and lines represent the deviation of the three Euler angles ( $\phi$ ,  $\theta$  and  $\varphi$ ) from the correct ones ( $0^\circ$ ) at each tilt angle. These angular errors were taken into account in the multi-slice simulations. **b**, The angular errors were correctly refined in the 3D reconstruction of the 55 multi-slice images using RESIRE (Methods). After the

angular refinement, the largest error is only  $0.2^\circ$ . **c, d**, Comparison between a representative experimental (after denoising) (**c**) and a multi-slice (**d**) image at  $0^\circ$ . To account for the source size and incoherence effects, each multi-slice image was convolved with a Gaussian function (Methods). **e**, Histogram of the deviation of the atomic positions between the experimental atomic model and that obtained from 55 multi-slice images. The peak, mean and root-mean-square deviation of the histogram are 6 nm, 15 nm and 21 pm, respectively. Scale bar, 2 nm.



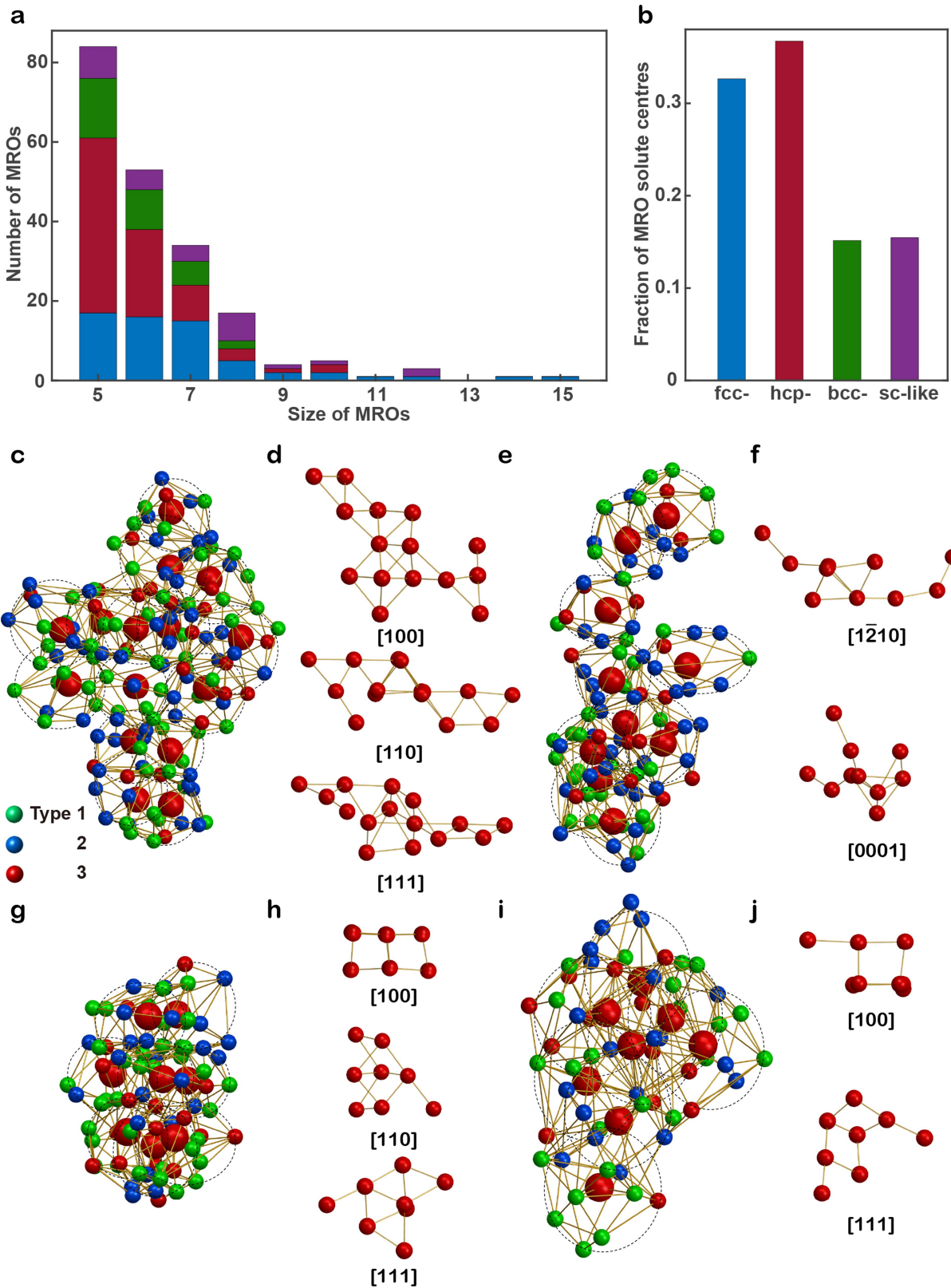
**Extended Data Fig. 5 | 3D distribution of the crystal nuclei in the glass-forming nanoparticle, partial coordination numbers and Voronoi polyhedra of the solute-centre clusters.** **a**, 3D distribution of the atoms with a normalized BOO parameter  $\geq 0.5$ , revealing that 15.46% of the total atoms form crystal nuclei in the nanoparticle. **b**, Normalized partial coordination numbers

of type-1, -2 and -3 atoms. **c**, 3D distribution of the 2,682 solute centres (red dots) that are between the first (3.78 Å) and the second (6.09 Å) minimum of the PDF curve (Fig. 1g). **d**, Ten most abundant Voronoi polyhedra of the solute-centre clusters.



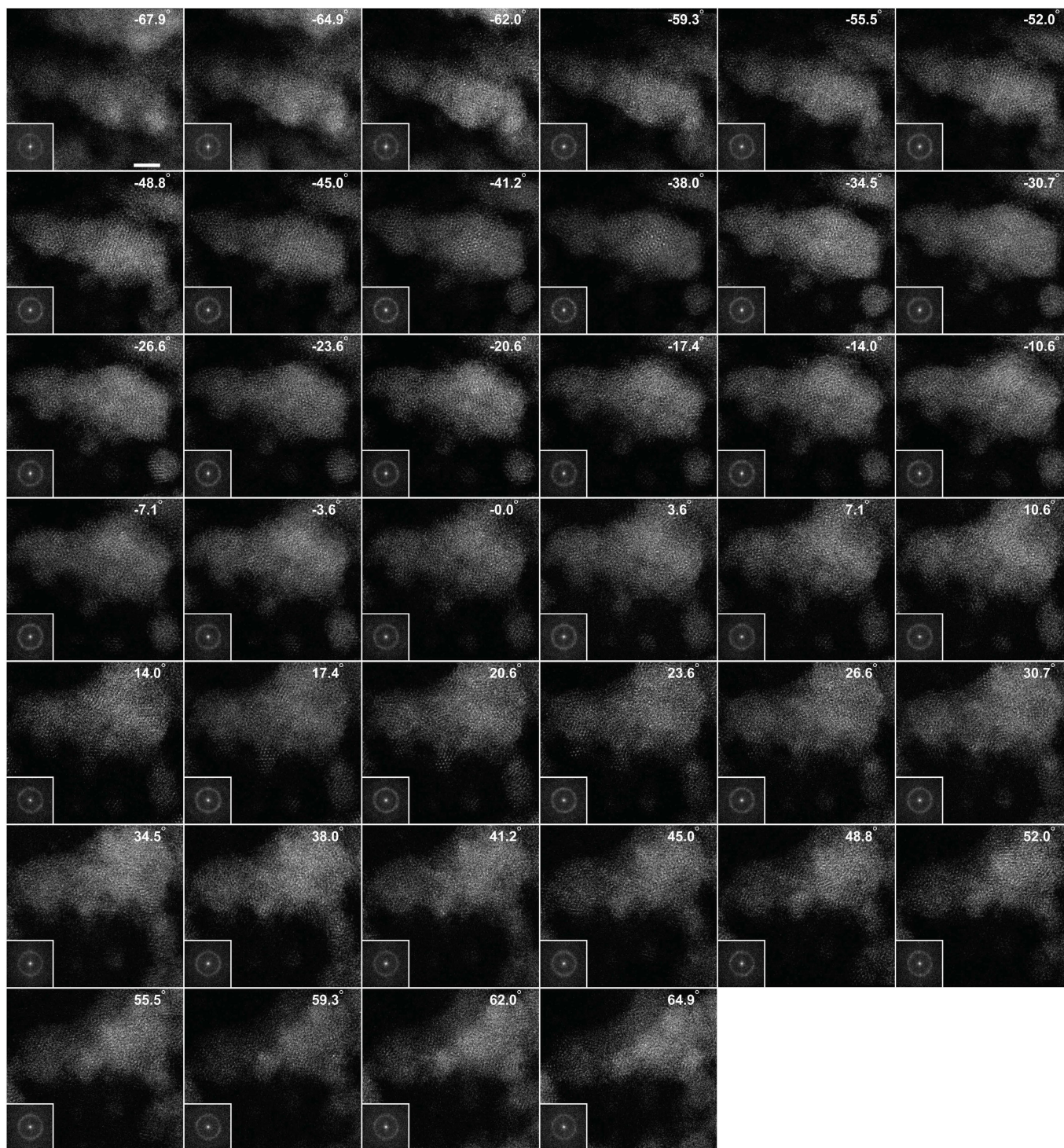
**Extended Data Fig. 6 | Identification of MROs with a 1-Å radius cut-off.**  
**a**, Histogram of the four types of MRO—fcc- (blue), hcp- (red), bcc- (green) and sc-like (purple)—as a function of size (that is, the number of solute centres).  
**b**, Population of the solute-centre atoms for the four types of MRO.

**c–j**, Representative fcc- (**c**), hcp- (**e**), bcc- (**g**) and sc-like (**i**) MROs, containing 23, 18, 10 and 27 solute centres (large red spheres), respectively. The solute centres are orientated along the fcc (**d**), hcp (**f**), bcc (**h**) and sc (**j**) zone axes.

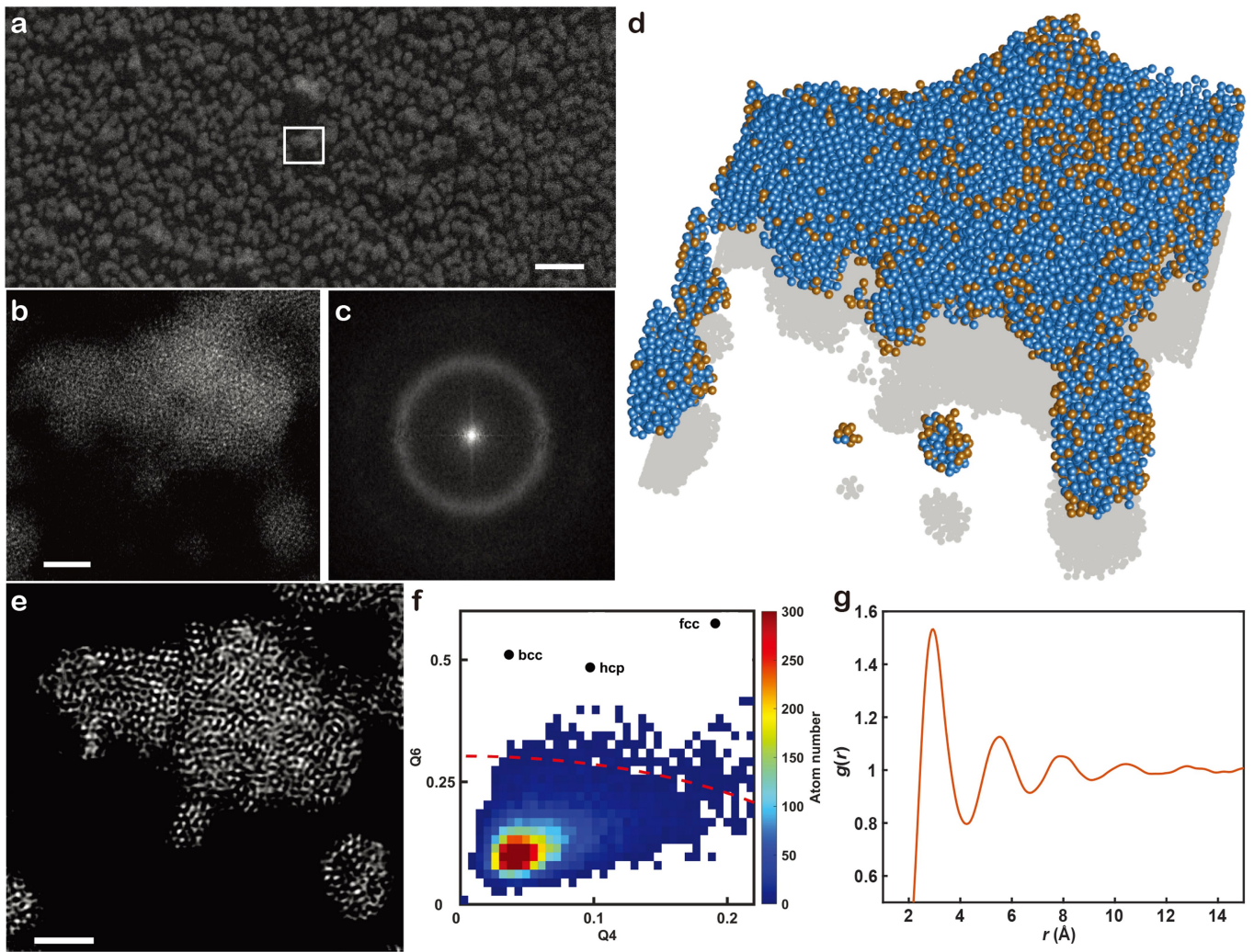


**Extended Data Fig. 7 | Identification of MROs with a 0.5-Å radius cut-off.**  
**a**, Histogram of the four types of MRO—fcc- (blue), hcp- (red), bcc- (green) and sc-like (purple)—as a function of size. **b**, Population of the solute-centre atoms for the four types of MRO. **c–j**, Representative fcc- (**c**), hcp- (**e**), bcc- (**g**) and

sc-like (**i**) MROs, containing 15, 10, 8 and 8 solute centres (large red spheres), respectively. The solute centres are orientated along the fcc (**d**), hcp (**f**), bcc (**h**) and sc (**j**) zone axes.



**Extended Data Fig. 8 | Tomographic tilt series of an amorphous CuTa thin film.** ADF-STEM images of a portion of the CuTa thin film. The insets show the 2D power spectra of the experimental images, in which the amorphous halo are clearly visible. Scale bar, 2 nm.



**Extended Data Fig. 9 | Determination of the 3D atomic structure of the amorphous CuTa thin film.** **a**, Large-field-of-view image of amorphous CuTa. **b**, Magnified image of the region in the white square in **a**. **c**, Average 2D power spectrum of all the experimental images. **d**, 3D atomic model of a portion of the CuTa thin film with a total of 1,808 Cu (gold) and 12,774 Ta (blue) atoms, determined from the tilt series shown in Extended Data Fig. 8 (Methods). Because the CuTa film is thinner than ~6 nm, 40 experimental images are

sufficient to produce a good 3D reconstruction. **e**, A 2-Å-thick internal slice of the 3D reconstruction of the amorphous CuTa thin film, showing the disordered atomic structure. **f**, Local BOO parameters of the 3D atomic model, where only 0.47% of the total atoms with a normalized BOO parameter  $\geq 0.5$  form crystal nuclei. **g**, PDF of the disordered atoms with a normalized BOO parameter  $< 0.5$ . Scale bars, 30 nm (**a**) and 2 nm (**b**, **e**).

# Article

Extended Data Table 1 | AET data collection, processing, reconstruction, refinement and statistics

	Particle 1	Particle 2	Particle 3	Particle 4	Particle 5	Particle 6	Particle 7	CuTa film
<b>Data collection and processing</b>								
Voltage (kV)	200	200	200	200	200	200	200	300
Convergence semi-angle (mrad)	25	25	25	25	25	25	25	17.1
Probe size (Å)	0.8	0.8	0.8	0.8	0.8	0.8	0.8	0.7
Detector inner angle (mrad)	38	38	38	38	38	38	38	30
Detector outer angle (mrad)	190	190	190	190	190	190	190	195
Depth of focus (nm)	8	8	8	8	8	8	8	14
Pixel size (Å)	0.347	0.347	0.347	0.347	0.347	0.347	0.347	0.322
# of images	55	51	54	54	53	53	55	40
Tilt range (°)	-69.4 +72.6	-69.3 +63.4	-72.5 +63.4	-71.7 +69.4	-69.6 +74.0	-71.7 +69.4	-69.5 +72.0	-67.9 +64.9
Total electron dose ( $10^5 e^-/\text{Å}^2$ )	9.5	7.1	7.6	7.6	7.4	7.4	7.7	2.4
<b>Reconstruction</b>								
Algorithm	RESIRE							
Oversampling ratio	4	4	4	4	4	4	4	3
Number of iterations	200	200	200	200	200	200	200	500
<b>Refinement</b>								
$R_1$ (%) <sup>a</sup>	9.54	12.32	11.57	10.90	9.38	7.62	7.65	10.58
R (%) <sup>b</sup>	6.45	9.87	8.98	7.68	7.46	5.66	5.73	8.61
B' factors (Å <sup>2</sup> )								
Type 1 atoms	48.9	55.4	48.4	44.0	35.5	55.6	35.5	45.2
Type 2 atoms	46.4	47.3	44.3	44.0	34.5	58.0	34.5	45.2
Type 3 atoms	52.3	37.4	39.6	40.9	34.6	42.1	34.6	NA
<b>Statistics</b>								
# of atoms								
Total	18356	2063	3447	4661	7739	6648	6037	14582
Type 1	8322	648	1116	1079	2158	1579	1446	1808(Cu)
Type 2	6896	937	1327	1906	2750	2430	2045	12774(Ta)
Type 3	3138	478	1004	1676	2831	2639	2546	

<sup>a</sup>The  $R_1$  factor is defined as in equation (5) of ref. <sup>41</sup>.

<sup>b</sup>The R factor is defined as in equation (4).